https://doi.org/10.5194/egusphere-2025-6390
Preprint. Discussion started: 30 December 2025

Vertical Mode and Cyclonic Eddy Encounters Govern Internal Tide Propagation and Intermodal Cascades: High-resolution Eddy Permitting Simulations

Fabius Kouogang [1,2], Ariane Koch-Larrouy[1], Xavier Carton[3], Moacyr Araujo[2]

[1]CECI, Université de Toulouse, CERFACS/CNRS/IRD, Toulouse, France
[2]Departamento de Oceanografia, Universidade Federal de Pernambuco, DOCEAN/UFPE, Recife, Brazil
[3]Physical and Spatial Oceanography Laboratory, European Institute for Marine Studies, University of WesternBrittany, Plouzane, France

Correspondence to: Fabius Kouogang (fabius.cedric@yahoo.fr)

Abstract. The interaction between internal tides (ITs) and mesoscale features plays a key role in ocean energy dissipation. Understanding how IT energy is transformed in energetic western boundary regions remains a central challenge, particularly in regions of vigorous mesoscale activity.

To this aim, we apply vertical mode decompositions to the flow from high-resolution (3 km) NEMO-AMAZON36 simulations during September-December 2015. This study shows that the IT vertical mode and the precise point of IT-eddy encounter determine whether the IT energy propagates freely, deviates, or is trapped, and how topography and coherent eddies synergistically scatter energy between baroclinic modes off the Amazon shelf.

Three representative interaction cases, each captured in a separate 25 hour snapshot, were examined: undisturbed propagation until crossing the Ceará Rise seamount, interaction with a cyclonic eddy (CE) core, and interaction with a CE eastern periphery. The principal findings establish two points.

First, an IT response (propagation, deviation or scattering) is dually controlled by its vertical mode and the mesoscale encounter properties. In the absence of a strong eddy, the Mode-1 IT propagates as a coherent beam with a long propagation range (O (1100 km)). In the presence of a strong CE, however, the IT beams are disrupted, preventing sustained long-range transmission. Within the eddy core, the Mode-1 IT is coherently refracted northward (~ 35° relative to its northeastward incident direction) while maintaining high energy fluxes exceeding 200 W m^{-1}. At the CE periphery, Mode-1 is diffracted into two distinct branches, with one propagating northward (~39°) and the other eastward (~35°). In contrast, the IT higher modes are highly susceptible to blocking and trapping: Mode-2 energy, despite initial amplitudes comparable to Mode-1, is completely arrested at the CE-seamount interface, while Mode-3 remains weak (below 200 W m^{-1}) and less propagative.

Second, intermodal energy transfer is governed by a hierarchical synergy between the seamount and CE's background flow. The seamount drives a forward energy cascade (O (10^{-8} W m kg^{-1})) from the Mode-1 IT to higher modes. In contrast, the CE's strong horizontal shear triggers a competing inverse energy cascade (O (10^{-8} W m kg^{-1})) from the background flow to the IT modes. This interaction is critical for the extreme damping of Mode-2 and explains the observed redistribution of energy fluxes.

These results provide mechanistic insight into the fate of IT energy in complex oceanic environments and advance understanding of multi-scale ocean dynamics.

https://doi.org/10.5194/egusphere-2025-6390
Preprint. Discussion started: 30 December 2025

1 Introduction

Internal tides (ITs)—internal waves at tidal frequencies—are generated when barotropic tides interact with topography, forcing vertical displacements of the stratified water column (Garrett and Kunze, 2007; Kelly and Nash, 2010; Buijsman et al., 2012; Zhao, 2014; Chen et al., 2022). They enhance turbulent mixing and influence deep-water circulation (Wunsch and Ferrari, 2004; Kunze, 2017).

High-mode ITs, characterized by short wavelengths and large vertical shear, typically dissipate near their generation sites (Vic et al., 2019; Koch-Larrouy et al., 2015; Kouogang et al., 2025). In contrast, low-mode ITs propagate thousands of kilometers, redistributing tidal energy and acting on open-ocean mixing (Zhao, 2017; Alford et al., 2019; Wang et al., 2021; Kouogang et al., 2025). During their propagation, ITs can interfere with other tidal beams (e.g., tidal beams from other sources), interact with oceanic flows (e.g., subtidal currents, mesoscale eddies) and topography (e.g., seamounts, ridges), generating nonlinear internal solitary waves (ISWs) (Pereira et al., 2007; Zhang et al., 2014; Kelly and Lermusiaux, 2016; Wang et al., 2021; Xu et al., 2021; Wang et al., 2024; Li et al., 2024). Low-mode ITs can be scattered into higher modes by bathymetric roughness (Johnston and Merryfield, 2003; Mathur et al., 2014). These multiscale interactions cause IT incoherence and nonstationarity, challenging satellite detection (Zaron and Egbert, 2014; Savage et al., 2020).

Mesoscale eddies (MEs)—comprising both anticyclonic (AEs) and cyclonic (CEs) types—often possess horizontal scales comparable to those of low-mode ITs. This scale similarity allows MEs to alter oceanic stratification and currents, thereby influencing IT generation, propagation, and inter-modal energy redistribution through processes such as scattering, refraction, trapping, and damping (Dunphy and Lamb, 2014; Clément et al., 2016; Dunphy et al., 2017; Guo et al., 2023; Wang and Legg, 2023). MEs can enhance or weaken the topography scattering of ITs, causing spatial divergence (Li et al., 2024). Low-mode ITs can also be refracted or trapped by background currents like the looping and leaping Gulf Stream (Duda et al., 2018; Kelly and Lermusiaux, 2016; Kelly et al., 2016), Kuroshio (Cao et al., 2022; Xu et al., 2021; Chen et al., 2022) and Brazil Current (Pereira et al., 2007), changing their direction of propagation (Huang et al., 2018). Scattering by topography and background circulation to higher modes can redistribute energy toward more dissipative pathways (Lahaye et al., 2020; Fan et al., 2024).

Although the IT responses to background circulation (stratification, currents, and eddies) are well-documented on seasonal and interannual timescales (Pereira et al., 2007; Nash et al., 2012; Tchilibou et al., 2020, 2022), their variability at shorter, daily timescales remains less explored. Our study addresses this gap by investigating the rapid variability of IT responses to MEs off the Amazon shelf.

The region off the Amazon shelf is a dynamic region with a strong western boundary current (North Brazil Current, NBC), receiving large amounts of freshwater from the Amazon and Para Rivers. The area is also marked by high mesoscale activity (MEs), and the presence of seamounts, ITs, and ISWs (Fig. 1). The NBC flows northwestward, exhibiting a seasonal double retroflection eastward, a first one into the North Equatorial Counter-Current (NECC) at about 5–8◦ N near 50◦ W, and a second one into the Equatorial Undercurrent (EUC) in winter–spring (Didden and Schott, 1993). Shear instabilities within these currents and their interaction with the Amazon slope generate the CEs and AEs (NBC rings) in this region (Fratantoni and Glickson, 2002; Barnier et al., 2001; Silva et al., 2009). From August to December (ASOND), mean currents and eddy kinetic energy (EKE) are stronger, and the pycnocline is deeper and weaker than during the March-to-July (MAMJJ) season (Aguedjou et al., 2019; Barbot et al., 2021; Tchilibou et al., 2022). Generated at multiple sites (A to E, Fig. 1) along the Amazon

https://doi.org/10.5194/egusphere-2025-6390
Preprint. Discussion started: 30 December 2025

shelf break (Tchilibou et al., 2022; Assene et al., 2024; Magalhaes et al. 2016), ITs from the most energetic sites (A and D, Fig. 1) can either propagate over long distances or interact with other processes to potentially disintegrate into ISWs, which have been observed via in situ measurements (Brandt et al., 2002), SAR imagery (Magalhães et al., 2016), MODIS (De Macedo et al., 2023), and SWOT data (Goret et al., 2025). This makes the region an ideal laboratory for studying the tidal variability of IT responses during the propagation of tidal flux.

Using numerical modeling, Tchilibou et al. (2022) reported that the M2 coherent baroclinic tidal flux propagates more northward during MAMJJ in the region off the Amazon shelf. During ASOND, however, it becomes incoherent—branching and deviating near 6°N—due to strong interactions with MEs and background currents off the Amazon shelf. This variability in flux behavior (e.g., free propagation, refraction, branching) during ASOND may result from the interaction of the coherent flux with MEs, sheared currents (e.g., NECC), changes in stratification, topography (e.g., Ceará Rise seamount, Mid-Atlantic ridge; Fig. 1), other internal wave sources, or coupled processes.

Motivated by the complex mesoscale interplay off the Amazon shelf, we investigate the fate of IT within this dynamic environment at daily timescales from the realistic model outputs. Specifically, we examine whether ITs propagate freely, are deviated, or become trapped by mesoscale features. We further determine whether these outcomes depend on the vertical modes of ITs or the properties of the MEs, distinguishing, for instance, between interactions at a CE core versus its periphery. Finally, we explore the synergistic roles of topography (e.g., Ceará Rise seamount) and CEs in governing modal energy transfers.

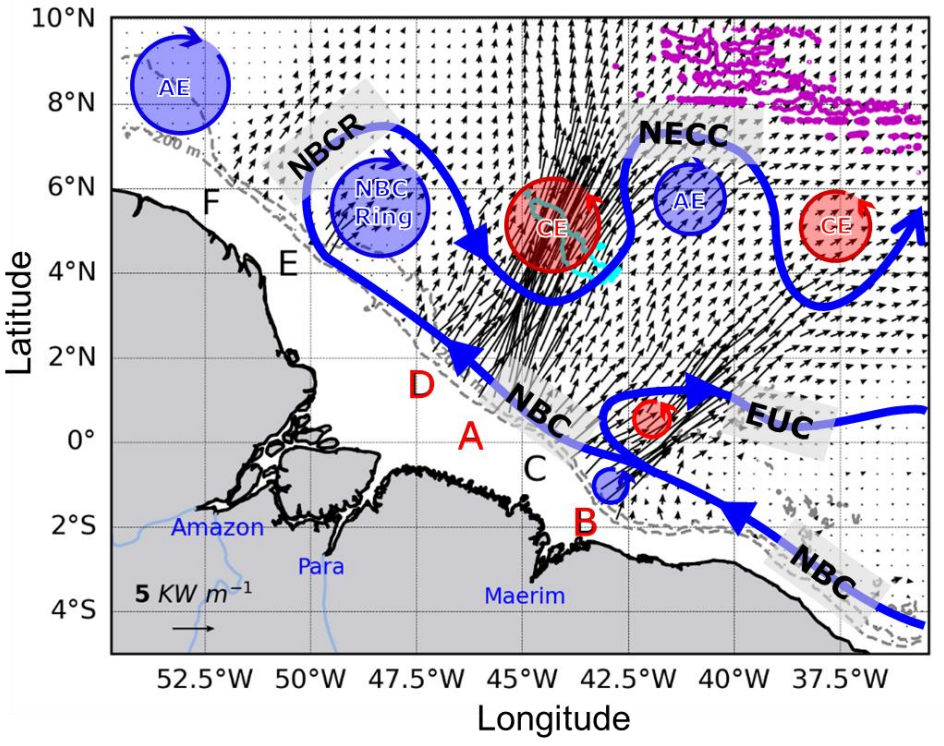

https://doi.org/10.5194/egusphere-2025-6390
Preprint. Discussion started: 30 December 2025

Figure 1. Internal tide generation and propagation, and regional circulation off the Amazon shelf. Key IT generation sites (A–F) are marked along the shelf break slope, with the three primary sites (A, B, D) highlighted in red. The associated M_2 baroclinic energy flux, represented by black arrows, is the 25-hour mean depth-integrated flux from the September-December (SOND) 2015 period. The schematic background circulation includes the North Brazil Current (NBC), its retroflection (NBCR), North Equatorial Countercurrent (NECC), and Equatorial Undercurrent (EUC) (solid blue lines). Mesoscale eddies are indicated by cyclonic (CEs, red circles) and anticyclonic eddies (AEs, blue circles), the latter including the NBC Ring. Topography is detailed with the 200 m and 2000 m isobaths (grey lines) and specific features outlined by their 3500 m isobath (Ceará Rise seamount: cyan contour; Mid-Atlantic ridge: magenta contour).

2 Methodology

2.1 High-resolution Numerical Modeling

We use output from the Nucleus for European Modeling of the Ocean (NEMO) model, specifically the AMAZON36 configuration (Madec et al., 2019). This high-resolution (1/36°, ~3 km) model is designed for the western tropical Atlantic (54.7° W–35.3° W, 5.5° S–10° N) and features 75 vertical layers, with 23 levels in the upper 100 m to resolve near-surface processes. This configuration capably resolves low-mode ITs and accurately represents the topography critical to their generation and propagation from the Amazon shelf break (Tchilibou et al., 2022; Assene et al., 2024).

The model employs a third-order upstream biased scheme for momentum advection and a second-order flux-corrected transport scheme for tracers (Zalesak, 1979). Subgrid-scale parameterizations include Laplacian isopycnal tracer diffusion (20 $m^2\ s^{-1}$) and a k-ε turbulent closure scheme for vertical mixing. Lateral boundaries are free-slip and bottom friction is quadratic (drag coefficient: 2.5×10^{-3}). Temporal integration uses a leapfrog scheme with an Asselin filter and a baroclinic time step of 150 s, while a time-splitting technique handles the free surface.

The model bathymetry was extracted from GEBCO (General Bathymetric Chart of the Ocean) 2020 data, surface conditions from the ERA5 reanalysis (Hersbach et al., 2020), and river runoff from the ISBA (Interaction Sol-Biosphère-Atmosphère model: https://www.umr-cnrm.fr/spip.php?article146&lang=en, last access: 20 September 2024). Open boundary conditions are provided by the FES2014 tidal atlas (15 constituents: M_2, S_2, N_2, K_2, $2N_2$, MU_2, NU_2, L_2, T_2, K_1, O_1, Q_1, P_1, S_1, and M_4; Lyard et al., 2021) and hydrographic/velocity data from the MERCATOR-GLORYS12v1 reanalysis (Lellouche et al., 2018).

The simulation runned for 11 years until December 2015 and provides three-dimensional, hourly AMAZON36 output. This dataset has previously been used to study IT interactions with background circulation and stratification (Barbot et al., 2021; Tchilibou et al., 2022; Assene et al., 2024; Kouogang et al., 2025).

For this study, we focus on the period from September to December (SOND) 2015, when stronger mean currents and EKE contribute to more incoherent ITs (Tchilibou et al., 2022). To analyze the rapid variability of IT responses to MEs like CEs, we examine 25-hour segments within this season.

2.2 Internal Tides and Mesoscale Activity

Our analysis for each 25-hour window of AMAZON36 outputs during the SOND period involves several steps: extracting the M2 IT constituent, separating the barotropic and baroclinic components, projecting the baroclinic

https://doi.org/10.5194/egusphere-2025-6390
Preprint. Discussion started: 30 December 2025

components onto vertical modes, extracting MEs and characterizing their properties, and examining the mean background current pattern and topographic features.

2.2.1 Undecomposed IT Energy equations

First, to examine the variability of IT responses to MEs, we explore all 25-hour snapshots of IT energy flux from the AMAZON36 output during the SOND period. Following the method of Kelly et al. (2010), barotropic and baroclinic tidal constituents were separated. This separation is performed directly by the NEMO model to ensure accuracy, providing the total energy for all resolved propagation modes at a given tidal frequency (Tchilibou et al., 2022). Our analysis focuses solely on the M2 harmonic, the dominant tidal constituent in this region (Fassoni-Andrade et al., 2023).

The energy budget for IT can be expressed from the following equations (Wang et al., 2016; Buijsman et al., 2012; Kerry et al., 2013; Tchilibou et al., 2022; Siyanbola et al. 2024):

$$\nabla_h \cdot \boldsymbol{F} + D + R = C \qquad (1)$$

In contrast to energy budgets decomposed into vertical modes, we refer to these as the undecomposed IT energy equations. Here, $\nabla_h \cdot \boldsymbol{F}$ is the divergence of the depth-integrated energy flux, $\boldsymbol{F} = (F_x, F_y)$ the energy flux vector, C, represents the depth-integrated barotropic-to-baroclinic energy conversion, and D is the depth-integrated energy dissipation term. The term R includes the energy tendency term, implicit horizontal dissipation, wave-mean flow and wave-wave interaction terms, and other offline computation errors. $\nabla_h = (\partial/\partial x, \partial/\partial y)$ is the horizontal gradient operator.

In the following, a particular attention is given to depth-integrated and time-averaged energy flux term $\boldsymbol{F}$, which was defined as (Tchilibou et al., 2022; Assene et al. 2024):

$$[\boldsymbol{F}_{bc}, \boldsymbol{F}_{bt}] = [\int_{-H}^{\eta} \boldsymbol{u}_{bc}\ p_{bc}\ dz, \boldsymbol{u}_{bt}\ p_{bt}\ ], \qquad (2)$$

where $\boldsymbol{u} = (u, v)$ is the horizontal baroclinic tidal velocity vector, and p_{bt} the barotropic tidal pressure. Here, the subscripts bt and bc denote barotropic and baroclinic components, respectively. η is the sea surface height.

2.2.2 Projection of IT Motions Onto Vertical Modes

Second, to investigate whether the IT responses to MEs is mode-dependent and to examine potential inter-modal energy transfer, we project the M_2 tidal constituent onto a set of vertical modes for selected 25-hour snapshots that capture ME-induced IT responses. This selective approach substantially reduces the computational cost associated with processing high-resolution 3D data for all 25-hour windows during the SOND period.

Vertical Mode Decomposition

For each selected snapshot, we first extract the M2 harmonic via harmonic analysis. We then decompose the tidal currents and pressure using a locally computed set of vertical modes. This method provides a more accurate separation of barotropic and baroclinic tides than simpler approaches (Kelly, 2016; Lahaye et al., 2020; Lahaye et al., 2024; Siyanbola et al. 2024). The vertical modes are obtained by solving the standard Sturm-Liouville

https://doi.org/10.5194/egusphere-2025-6390
Preprint. Discussion started: 30 December 2025

eigenvalue problem at each horizontal grid point, assuming a flat bottom, a free surface, horizontally homogeneous stratification (based on the time-mean buoyancy frequency, $\overline{N^2}$), and no background flow (Gerkema and Zimmerman, 2008; Bella et al., 2024):

$$\partial_z\left(\frac{\partial_z \Phi_n}{\overline{N^2}}\right) + \frac{\Phi_n}{c_n^2} = 0, \quad (3)$$

with the boundary conditions:

$\partial_z \Phi_n = 0$ at z = -H, and g $\partial_z \Phi_n + \overline{N^2}\,\Phi_n = 0$ at z = $\bar{\eta}$, (4)

where ∂_z denotes the partial derivative in z-direction, Φ_n is the horizontal velocity/pressure eigenfunction for mode n, c_n is the modal phase speed, H is the seafloor depth, and g is gravity. The associated vertical velocity/buoyancy eigenfunction, φ_n, is given by:

$$\partial_z \varphi_n = \Phi_n, \text{ and } \partial_z \Phi_n = -\frac{\overline{N^2}}{c_n^2}\varphi_n. \quad (5)$$

The vertical modes satisfy the orthogonality condition (Kelly, 2016; Lahaye et al., 2024; Bella et al., 2024):

$$\int_{-H}^{\bar{\eta}} \Phi_m \Phi_n \, dz = H\delta_{mn} \quad (6)$$

where δ_{mn} is the Kronecker delta and $\bar{\eta}$ is the time-averaged sea surface height.

We solved Equation 3 for the first 10 modes (n = 0, 1, ..., 9) at each grid point, where n = 0 represents the barotropic mode. In this study, the analysis of energy flux focuses primarily on the first three baroclinic modes, which are the most dynamically significant at the model's resolution (~ 3 km).

The horizontal velocity $\boldsymbol{u}$ and pressure p fields are projected onto these modes to obtain the depth-independent modal amplitudes:

$$[\boldsymbol{u}_n(\mathbf{x}, t),\ p_n(\mathbf{x}, t)] = \frac{1}{H}\int_{-H}^{\bar{\eta}} [\boldsymbol{u}(\mathbf{x}, z, t),\ p(\mathbf{x}, z, t)]\, \Phi_n(\mathbf{x}, z)\, dz, \quad (7)$$

with $\mathbf{x}$ = (x, y) denoting the horizontal direction.

The full 3D structure of $\boldsymbol{u}_n$ fields for each mode can be reconstructed as (Li et al., 2024):

$$\boldsymbol{u}_n(\mathbf{x}, z, t) = \boldsymbol{u}_n(\mathbf{x}, t)\, \Phi_n(\mathbf{x}, z) \quad (8)$$

Modal Energy Budget

To analyze the inter-modal energy transfer/scattering and redistribution, we examine the terms of the modal energy budget of a given mode interacting with physical features such as topography and mesoscale flow (Fan et al., 2024; Bella et al., 2024; Kelly, 2016; Kelly and Lermusiaux, 2016):

https://doi.org/10.5194/egusphere-2025-6390
Preprint. Discussion started: 30 December 2025

$$\nabla_h \cdot \boldsymbol{F}_m + D_m + \Psi_m = \sum_n (C_{mn} + A_{mn} + H_{mn} + V_{mn} + B_{mn}). \quad (9)$$

Here:

- C_{mn} is the nonlinear scattering (from mode m > 0 into mode n) of energy by topography and stratification.
- A_{mn} represents the advection of the ITs by the background flow and MEs.
- H_{mn} and V_{mn} represent the effect of the horizontal and vertical shear of the background flow, respectively.
- $\boldsymbol{F}_m = H\, p_m\, \boldsymbol{u}_m$ is the depth-integrated and time-averaged baroclinic energy flux for mode n.
- B_{mn} consist of the three-way interaction term and the horizontal gradient of the buoyancy field.
- Ψ_m consists of the energy tendency terms.
- D_m is the dissipation term of modal energy budget, which also includes interactions with unresolved modes, other physical dissipation processes leading to local dissipation (Alford & Zhao, 2007), and other offline computation errors.

A previous seasonal-scale study by Bella et al. (2024) found the nonlinear coupling terms C_{mn}, A_{mn}, H_{mn}, and V_{mn} to be dominant across the North Atlantic basin. For our investigation on a daily timescale, a preliminary analysis identified C_{mn} and H_{mn} as the dominant terms in our study region. We therefore focus on estimating these dominant couplings terms as defined by Bella et al. (2024):

$$C_{mn} = \langle H\, p_m\, \boldsymbol{u}_n \cdot T_{nm} - H\, p_n\, T_{mn} \cdot \boldsymbol{u}_m \rangle, \quad (10)$$

$$H_{mn} = \langle - H\, (U^{\nabla}{}_{mn}\, \boldsymbol{u}_n) \cdot \boldsymbol{u}_m \rangle, \quad (11)$$

with $T^{mn} = \frac{1}{H} \int_{-H}^{\bar{\eta}} \Phi_m \nabla_h (\Phi_n)\, dz$, $(U^{\nabla}{}_{mn})_{ij} = \frac{1}{H} \int_{-H}^{\bar{\eta}} \Phi_m\, \Phi_n \frac{\partial \bar{U}_{h,i}}{\partial x_j}\, dz$.

Here, the angle bracket $\langle \cdot \rangle$ denotes the average over a M2 tidal period, $\bar{U}_h = (\bar{U}, \bar{V})$ is the time-averaged total horizontal velocity vector. $\frac{\partial \bar{U}_{h,i}}{\partial x_j}$ is the tensor.

The modal horizontal kinetic energy (HKE_n) of M2 IT is estimated as (Kelly et al., 2012; Fan et al., 2024):

$$HKE_n = \frac{\rho_o H}{2} \langle u_n{}^2 + v_n{}^2 \rangle, \quad (12)$$

where ρ_0 is the reference density.

Symmetric–Antisymmetric Separation of Nonlinear Coupling Terms

The energy transfer matrices—including topographic scattering (C_{mn}) and (H_{mn})—are decomposed into symmetric and antisymmetric components, following the established methodology (Savage et al., 2020; Bella et al., 2024). For any general transfer matrix (X_{mn}), the standard mathematical definitions are: the antisymmetric component, $X^A{}_{mn} = ½ (X_{mn} - X_{nm})$, and the symmetric component, $X^S{}_{mn} = ½ (X_{mn} + X_{nm})$.

The antisymmetric component, $X^A{}_{mn}$, represents the internal reallocation of energy—specifically, the scattering or transfer of energy among the various IT vertical modes. Critically, this process conserves the total energy of the IT field, as it analytically redistributes energy across the system modes and spatial scales without introducing

https://doi.org/10.5194/egusphere-2025-6390
Preprint. Discussion started: 30 December 2025

a net gain or loss. For instance, the term C_{mn} is inherently antisymmetric and thus provides a canonical reference for conservative internal energy transfer.

Conversely, the symmetric component, X^{S}_{mn}, describes the net energy exchange between the IT and the low-frequency background flow. When integrated in a basin, this component acts as a source or sink for the IT system, quantifying the total energy gained from or lost to the slowly varying circulation (Bella et al., 2024).

The direction of energy transfer is interpreted from the sign of the matrix elements. Considering a specific mode m:

- For the full matrix X_{mn}, a negative value indicates a net forward transfer of energy from mode m to mode n, while a positive value indicates a net backward transfer from mode n to mode m.
- For the antisymmetric component X^{A}_{mn}, a negative value signifies a forward transfer from mode m to mode n of the IT field, and a positive value signifies a backward transfer.
- For the symmetric component X^{S}_{mn}, a negative value indicates a forward transfer from mode-m IT to the mode-n background flow, whereas a positive value indicates energy is transferred from the mode-n background flow to mode-m IT.

2.2.3 Eddy detection and structure

Third, to investigate whether the IT responses to MEs depend on eddy properties and location, we detected and characterized eddies from 25-hour mean snapshots of AMAZON36 output during the SOND period.

The mesoscale activity in this region during the 2015 ASOND period was previously assessed by Tchilibou et al. (2022). Their analysis, which compared the model's surface EKE with satellite data, showed reasonable agreement in both the spatial pattern and amplitude of the mean EKE, especially in regions dominated by the NECC.

Eddies were identified in our model outputs using the Okubo-Weiss parameter (W), chosen for its ability to detect coherent vortices on specific isopycnal surfaces or depths (Okubo, 1970; Weiss, 1991; 1991; Kurian et al., 2011; Xu et al. 2019). The W parameter is defined as:

$$W = S_n^2 + S_s^2 + \zeta^2, \tag{13}$$

where the normal strain (S_n) and shear strain (S_s), and the relative vorticity (ζ) are:

$$S_n = \frac{\partial u}{\partial x} - \frac{\partial v}{\partial y},\ S_s = \frac{\partial v}{\partial x} + \frac{\partial u}{\partial y},\ \zeta = \frac{\partial v}{\partial x} - \frac{\partial u}{\partial y}. \tag{14}$$

Regions where rotation dominates strain (W < 0) indicate potential eddy cores.

The detection of eddies on selected isopycnal surfaces (between 23 and 27 kg m^{-3} isopycnals) following the procedure of Kurian et al. (2011) and Xu et al. (2019). First, the W fields were smoothed using a 50 km × 50 km half-power filter to suppress small-scale noise. For each 25-hour mean snapshot, we then applied a constant threshold of $W_0 = -3 \times 10^{-11}$ s^{-2} to isolate vorticity-dominated regions ($W < W_0$). Closed contours corresponding to $W = W_0$ were identified, and each contour was subjected to a series of quality control criteria to be classified as an eddy: a shape error (deviation from a fitted circle) of less than 50%, a mean azimuthal velocity greater than 5 cm s^{-1}, and a radius larger than 50 km.

https://doi.org/10.5194/egusphere-2025-6390
Preprint. Discussion started: 30 December 2025

For each identified eddy, its thickness was defined as the vertical extent of its W_0 contours, and its center location was defined as the centroid of the closed W_0 contour. Detected eddies were classified as cyclonic or anticyclonic based on the sign (positive for CEs and negative for AEs) of their potential vorticity anomaly (PVA; Fig. 2a).

To analyze the eddy dynamical structure, we used the framework of rescaled potential vorticity (PV_r). This method filters out high-frequency wave noise to isolate the balanced mesoscale signal. The PVr is derived from the classical Ertel (1942) potential vorticity, rescaled by a reference stratification at rest, $\rho^*(z)$, following the approach of Morel et al. (2023, 2019) and subsequent studies (e.g., Delpech et al., 2020; Aguedjou et al., 2021; Ernst et al., 2023).

Its expression is:

$$PV_r = -(\nabla \cdot \boldsymbol{U} + f) \cdot \nabla \mathbf{Z}(\rho) = \nabla \cdot [(\nabla \cdot \boldsymbol{U} + f)\nabla \mathbf{Z}(\rho)], \quad (15)$$

where $\mathbf{Z}$ is a rescaling function defined by $\mathbf{Z}(\rho^*) = z$. ρ^* is defined by the adiabatically rearranged state of minimum potential energy, following the concept of Lorenz (1955) as formalized by Nakamura (1995) and Winters and D'Asaro (1996). ρ is the potential density and f, the local Coriolis parameter. An eddy dynamical core is then identified by its anomaly from the background planetary vorticity, $PVA = PV_r - f$, within a layer bounded by two isopycnals.

To distinguish subsurface eddies from surface-intensified ones, we classified them based on the isopycnal level of their core of PVA. Following the method of Kouogang et al. (2025), we used the base of the pycnocline (defined by ~26.5 kg m^{-3} isopycnal) as the boundary of the lower pycnocline depth. Eddies with their PVA core on isopycnals less dense than 26 kg m^{-3} were classified as surface-intensified eddies (Fig. 2b), while those with their core on denser isopycnals (> 26.5 kg m^{-3}) were classified as subsurface-intensified eddies as formalized by Aguedjou et al. (2021) in the tropical Atlantic Ocean. This classification scheme was applied to all eddies detected during the SOND period. This study focuses specifically on these surface-intensified eddies.

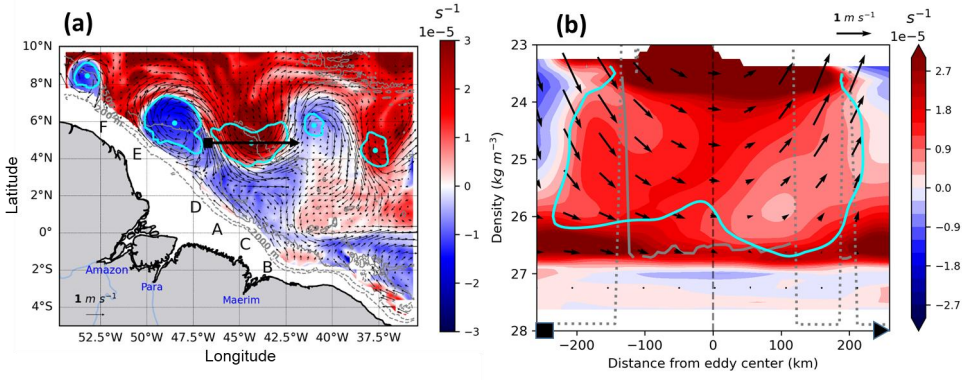

Figure 2. Detection and vertical structure of a representative ME (17 September 2015). (a) PVA (color shading) averaged within the 23–25.5 kg m^{-3} isopycnal layer (~50–160 m depth). Panel (a) shows detected eddy edges (cyan contours) and mean background currents (black arrows) along the 24 kg m^{-3} isopycnal. (b) Vertical cross-section of PVA along the transect in (a) (black arrow), passing through the core of a CE. The transect endpoints

https://doi.org/10.5194/egusphere-2025-6390
Preprint. Discussion started: 30 December 2025

are marked by a square (start) and triangle (end). The vertical dashed black line indicates the eddy centroid, black arrows show the CE-associated currents, and grey lines mark the upper (dotted) and lower (solid) thermocline limits. PVA and mean background currents fields were smoothed using a 50 km × 50 km half-power filter to suppress small-scale noise.

3 Results

In order to examine the variability of IT responses to MEs, particularly to CEs, we first present three representative cases of interactions between the (non-modal) baroclinic energy flux of the M2 IT and the detected eddy fields, identified from all 25-hour mean snapshots during SOND 2015. We then analyze the IT's vertical mode responses, focusing on the encounter location of the fluxes — originating from the most energetic generation sites A and D — with a CE along their path, and examine the potential modal energy transfer and redistribution.

3.1 Variability of IT responses to MEs: three distinct cases

Following the method described in Sects. 2.2.1 and 2.2.3 (Eqs. (1)-(2) and (13)-(15)), we identified three distinct cases from the SOND 2015 period for analysis, each occurring near a spring tide maximum to ensure comparably high and consistent tidal energy levels (Fig. 3). This setup minimizes the influence of tidal variability, allowing us to isolate the eddy-induced effects.

Figure 4 illustrates in the three relevant cases, the M_2 baroclinic energy flux, and MEs detected and their polarity given by the sign of PVA.

The selected cases are:

- No-Eddy case (NE, 24 November 2015): Energy flux from the primary generation sites (A and D) propagated freely, crossing the Ceará Rise seamount (~500 km from sites A and D; between 4°N–6° N, 45° W–42.5° W) and reaching the Mid-Atlantic ridge (~ 1100 km from sites A and D). A similar pattern was observed from site B (Fig. 4a).
- Cyclone Eddy Center case (CEC, 17 September 2015): Energy flux from sites A and D was refracted into a single beam at the core of a CE positioned (4.9° N, 44.4° W) above the seamount. Note that the seamount has an amplitude (h_{max}) of ~1000 m and width (w_{max}) of ~100km. Separately, flux from the less energetic site E was also refracted into a single beam, emanating from the center of a nearby AE (centered at 5.9° N, 48.5° W) (Fig. 4b).
- Cyclone Eddy Edge case (CEE, 29 September 2015): Energy flux from sites A and D was diffracted into multiple beams at the eastern periphery of a CE located (5.3° N, 45.0° W) on the northern flank of the seamount (Fig. 4c).

To determine whether these response patterns depend on the IT's vertical structure or eddy properties and location, we focus on the IT response to CEs and project the energy flux into vertical modes (Sect. 2.2.2). This approach enables us to examine the specific response of each vertical mode to the CE and potential modal energy redistribution and transfer resulting from these interactions.

https://doi.org/10.5194/egusphere-2025-6390
Preprint. Discussion started: 30 December 2025

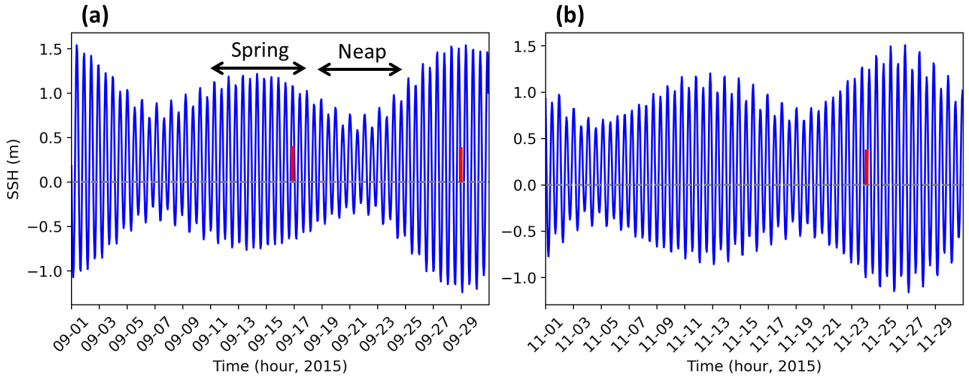

Figure 3. Sea surface height (SSH) from AMAZON36 simulations (station location: 1.29° N, 46.34° W) in (a) September and (b) November 2015. Red bars denote the three case study dates, and black arrows mark the spring-neap tidal cycle.

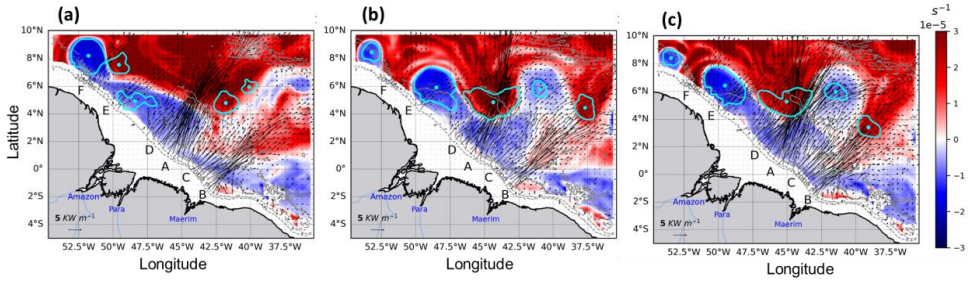

Figure 4. Depth-integrated M2 total baroclinic energy flux (black arrows) and isopycnally-averaged PVA (color shading), for the (a) NE, (b) CEC, and (c) CEE cases. All fields are 25-hour mean snapshots. The PVA is averaged within the 23–25.5 kg m^{-3} density layer (approximately 50–160 m). Detected eddies along the 24 kg m^{-3} isopycnal are overlaid, with edges (cyan contours) and centroids (cyan dots). The respective dates are 24 November 2015 (a), 17 September 2015 (b), and 29 September 2015 (c).

3.2 IT Responses to CEs

Following the method described in Sect. 2.2.2 (Eqs. (3)-(12)), we separately analyze the first three vertical modes of the M2 IT in the three cases.

3.2.1 NE Case: IT without Eddy

We first analyse the tidal energy diagnostics for the NE case to establish an eddy-free propagation baseline. Figures 5a-c maps the energy flux propagation and HKE for the first three modes, revealing distinct patterns for each.

Mode-1 energy propagation is highly dominant. The flux, generated constructively from sites A and D, forms a notably coherent beam that propagates northeastward (~37° azimuth) for over 1100 km with minimal deviation

https://doi.org/10.5194/egusphere-2025-6390
Preprint. Discussion started: 30 December 2025

(Fig. 5a). This long-distance propagation maintains a relatively constant HKE of 150–200 J m^{-2}, with a wavelength (λ_1) estimated between 90–125 km. In contrast, the Mode-2 flux propagates a significantly shorter distance (500–600 km, λ_2: 60–85 km) and terminates abruptly at the seamount (Fig. 5b). Mode-3 forms no coherent beams but appears as scattered patches extending only 50–100 km (λ_3: 35–50 km; Fig. 5c). Along their respective beams, Mode-1 and Mode-2 exhibit stronger energy flux amplitudes (>200 W m^{-1}) compared to Mode-3 (<200 W m^{-1}). The spatial distribution of these modal energy fluxes is consistent with the vertical structure of the corresponding baroclinic velocity profiles (Appendix A, Figs. A1–A2). A sharp Mode-2 damping is clearly visible over the seamount, while Mode-3 energy appears trapped over the seamount and ridge where the Mode-1 flux diminishes, suggesting that topographic features drive scattering to higher vertical modes.

To quantitatively assess the mechanisms responsible for this energy loss, we compute intermodal energy transfer terms (Eqs. (9)-(11)) and map only the dominant terms in Figures 5d-o. These dominant terms, of order of magnitude comparable (O (10^{-8} W m kg^{-1})), are topographic scattering term (C_{mn}, Eq. (10)), and the horizontal shear term (H_{mn}, Eq. (11)) of background flow. They then are separated into its antisymmetric and symmetric part for the analysis. All other background flow-induced energy transfer terms, such as advection and vertical shear, are negligible in comparison (O (10^{-10} W m kg^{-1}); figures not shown).

The analysis reveals a primary pathway of intermodal energy transfer driven by topographic scattering term (C_{mn}), which is antisymmetric by construction. Along the IT path from generation sites A and D, a dominant forward energy cascade occurs near major bathymetric features—the shelf break and seamount—with a magnitude of $|C_{mn}| \sim 4 \times 10^{-8}$ W m kg^{-1}. Specifically, energy is sequentially transferred from Mode-1 to Mode-2 IT (Fig. 5e, blue patches), and then from Mode-2 to Mode-3 IT (Figs. 5f, blue patches). In contrast, energy transfer is significantly weaker in the region downstream of the seamount (Fig. 5f, near-zero values). This area exhibits strong horizontal gradients in stratification (Appendix A, Fig. A2), suggesting that in the term Cmn, background stratification is not a primary mechanism for inter-modal energy transfer in this region.

Furthermore, direct energy transfer occurs between Mode-1 and Mode-3 IT over the ridge (Figs. 5d, blue patches), where Mode-1 loses energy towards Mode-3 IT. Between the seamount and shelf break, this relationship reverses, with Mode-1 IT gaining energy from Mode-3 (Fig. 5d, red patches). This direct backward energy transfer may result from other processes, notably the shear of background flow, whose influence is detailed below.

Decomposing the horizontal shear term H_{mn} (Figs. 5g–i) into its antisymmetric (Figs. 5j–l) and symmetric (Figs. 5m–o) components shows that its net influence ($|H_{mn}| \sim 4 \times 10^{-8}$ W m^{-1} kg^{-1}) is primarily due to the antisymmetric part. This latter facilitates energy transfer between IT modes. Indeed, energy is transferred from Mode-2 to Mode-1 IT (Figs. 5k, red patches) and from Mode-3 to Mode-1 IT (Figs. 5j, red patches) between the continental slope and the seamount. However, between Modes 2 and 3, the symmetric part of Hmn dominates the net effect, indicating an energy exchange with the background flow rather than between IT modes. Specifically, Mode-2 IT loses energy to the Mode-3 background flow between the continental slope and seamount (Figs. 5o, blue patches), and gains it back between the seamount and ridge (Figs. 5o, red patches).

https://doi.org/10.5194/egusphere-2025-6390
Preprint. Discussion started: 30 December 2025

In essence, in the NE case, coherent energy flux from sites A and D propagates until encountering major topographic features (seamounts and ridges). While Mode-1 IT energy propagates over long distances with amplitudes exceeding 200 W m^{-1}, the higher modes behave differently. Mode-2 IT energy, despite having a comparable amplitude to Mode-1, is effectively damped. In contrast, the weaker Mode-3 IT energy (< 200 W m^{-1}) becomes trapped by the topography. The interaction with topographic features, potentially enhanced by the background flow, triggers significant intermodal energy transfer on the order of 10^{-8} W m^{-1} kg^{-1}. This transfer is governed by two primary mechanisms: (1) topographic scattering drives a dominant forward energy cascade through the IT modes (Mode-1 → Mode-2 → Mode-3), and (2) the horizontal shear of the background flow facilitates a direct energy scattering from Mode-2 IT to the Mode-3 background flow.

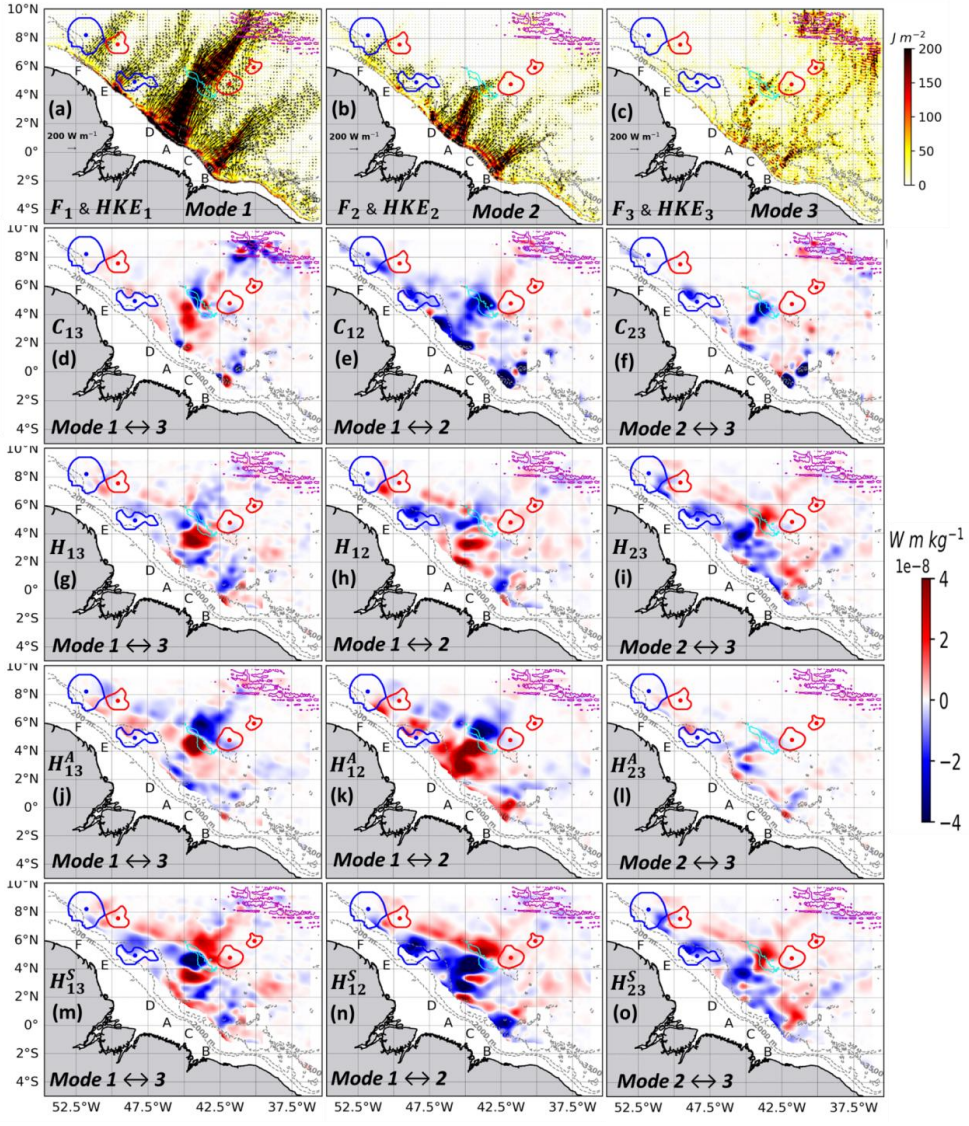

https://doi.org/10.5194/egusphere-2025-6390
Preprint. Discussion started: 30 December 2025

Figure 5. Tidal energy diagnostics for the NE case on 24 November 2015, averaged over a M2 tidal period. Panels (a–c) show the depth-integrated M2 baroclinic energy fluxes ($\mathbf{F}_m$; black arrows) and horizontal kinetic energy (HKE_m; color shading) for (a) mode-1 ($\mathbf{F}_1$, HKE_1), (b) mode-2 ($\mathbf{F}_2$, HKE_2), and (c) mode-3 ($\mathbf{F}_3$, HKE_3). Panels (d–f) present the effects of topographic scattering and stratification (Cmn; color shading) for (d) C_{13}, (e) C_{12}, and (f) C_{23}. Panels (g–i) show the net component of horizontal shear induced by the mean background flow (Hmn; color shading) for (g) H_{13}, (h) H_{12}, and (i) H_{23}. Panels (j–l) show the antisymmetric component of this horizontal shear (Hmn; color shading) for (j) H^A_{13}, (k) H^A_{12}, and (l) H^A_{23}. Panels (m–o) show the symmetric component of horizontal shear (Hmn; color shading) for (m) H^S_{13}, (n) H^S_{12}, and (o) H^S_{23}. All panels include the detected eddy edges (closed contours) and eddy centroids (dots) for anticyclones (blue) and cyclones (red). Topography is shown using the 200 m and 2000 m isobaths (grey contours), with specific features highlighted by the 3500 m isobath (seamount: cyan contour; Mid-Atlantic Ridge: magenta contour). The C_{mn} and H_{mn} fields were smoothed with a Gaussian filter ($\sigma = 7$ grid points) to aid interpretation.

3.2.2 CEC Case: IT Encountering a CE Core

We next examine IT responses when the energy flux from sites A and D encounter the core of a surface-intensified CE (CEC case, Fig. 2b). The CE, centered at 4.9° N, 44.4° W above the localized mid-seamount, has a radius of 157 km, maximum velocity 1.35 m s^{-1}, and a core bounded by 23–25.5 kg m^{-3} isopycnals extending ~150 m within the pycnocline.

Prior to interaction, the incident mode-1 IT energy fluxes converge and interfere. Upon encountering the CE core, this energy is refracted into a single beam (Fig. 6a), which emanates from the eddy center and propagates northward at approximately 35° from their northeastward incident direction. Both incident and refracted beams maintain comparable HKE of 150–200 J m^{-2} (Fig. 6a), though the refraction process locally confines the energy, leading to a reduction in HKE (25–50 J m^{-2}) in the northwestern lee of the eddy. Concurrently, the Mode-2 IT energy flux is blocked at the southern edge of the CE and seamount (Fig. 6b), while Mode-3 appears as scattered patches in the regions where Mode-2 is trapped (Fig. 6c), indicating active intermodal energy scattering. As in the NE case, Mode-1 and Mode-2 IT exhibit higher energy flux amplitudes (>200 W m^{-1}) along their beams than Mode-3 (<200 W m^{-1}) (Figs. 6a-c). The vertical structure of the along-transect baroclinic velocity further supports these results (Appendix A, Figs. A1, A3).

An analysis parallel to that conducted for the NE case identified the topographic scattering term (C_{mn}) and the horizontal shear term (H_{mn}) of the background flow as the dominant mechanisms responsible for the active energy scattering observed.

The analysis of the term C_{mn} in the CEC case reveals a distinct coupling pattern modulated by the CE core in conjunction with the seamount along the IT path from sites A and D. A dominant forward energy transfer ($|C_{mn}| \sim 4 \times 10^{-8}$ W m kg^{-1}) from Mode-1 to Mode-2 occurs near the shelf break (Fig. 6e, blue patches), consistent with the NE case (Fig. 5e). A significant shift occurs near the southern edge and core of the CE, where a dominant backward energy transfer is observed (with the exception of Mode-1 to Mode-3 IT). Here, energy is sequentially

https://doi.org/10.5194/egusphere-2025-6390
Preprint. Discussion started: 30 December 2025

gained by Mode-1 from Mode-2 (Fig. 6e, red patches near the southern edge and core of the CE) and by Mode-2 from Mode-3 (inverse cascade, Fig. 6f, red patches), while energy is simultaneously lost from Mode-1 to Mode-3 (direct forward transfer, Fig. 6d, blue patches).

Analysis of the background flow horizontal shear term (H_{mn}) shows that its magnitude ($|H_{mn}| \sim 4 \times 10^{-8}$ W m^{-1} kg^{-1}) is comparable to the topography scattering term as in NE case. In the CEC case, the net effect of Hmn (Figs. 6g-i) is primarily governed by its symmetric part (Figs. 6m-o), which facilitates energy exchange from the background flow to the IT modes. Specifically, between the shelf break and the southern edge of the CE, Mode-2 IT loses energy to the Mode-3 background flow (Fig. 6o, blue patches). Then, near the CE core and seamount, the background flow loses energy to the IT modes, with Mode-2 background flow energizing Mode-1 IT (Fig. 6n, red patches) and Mode-3 background flow energizing Mode-2 IT (Fig. 6o, red patches). However, between Mode-1 and Mode-3, the antisymmetric and symmetric parts of Hmn work in opposition (Figs. 6g,j,m), resulting in a near-zero net energy transfer. These overall patterns indicate a deflection of Mode-1 and Mode-2 IT, and provide strong evidence for a dominant energy pathway from the background flow to the IT modes driven by horizontal shear. This latter is coupled with direct forward energy transfer between IT modes driven by topographic scattering previously observed.

In summary, in the CEC case, the interaction with the CE core dictates distinct fates for IT modes. Mode-1 IT from sites A and D is not freely propagating but is primarily refracted into a single northward beam. In contrast, Mode-2 IT is blocked, and Mode-3 IT is scattered at the eddy edge and seamount. Energy flux amplitudes for Modes 1 and 2 exceed 200 W m^{-1} along their beams, whereas Mode-3 remains below this threshold. This interaction facilitates a significant energy transfer (O(~10^{-8} W m kg^{-1})) governed by a complex interplay of two mechanisms: 1) a dominant backward energy cascade, where horizontal shear transfers energy from the Mode-3 background flow to Mode-2 IT, and from the Mode-2 background flow to Mode-1 IT; and 2) a forward scattering, where topography directly transfers energy from Mode-1 to Mode-3 IT.

https://doi.org/10.5194/egusphere-2025-6390
Preprint. Discussion started: 30 December 2025

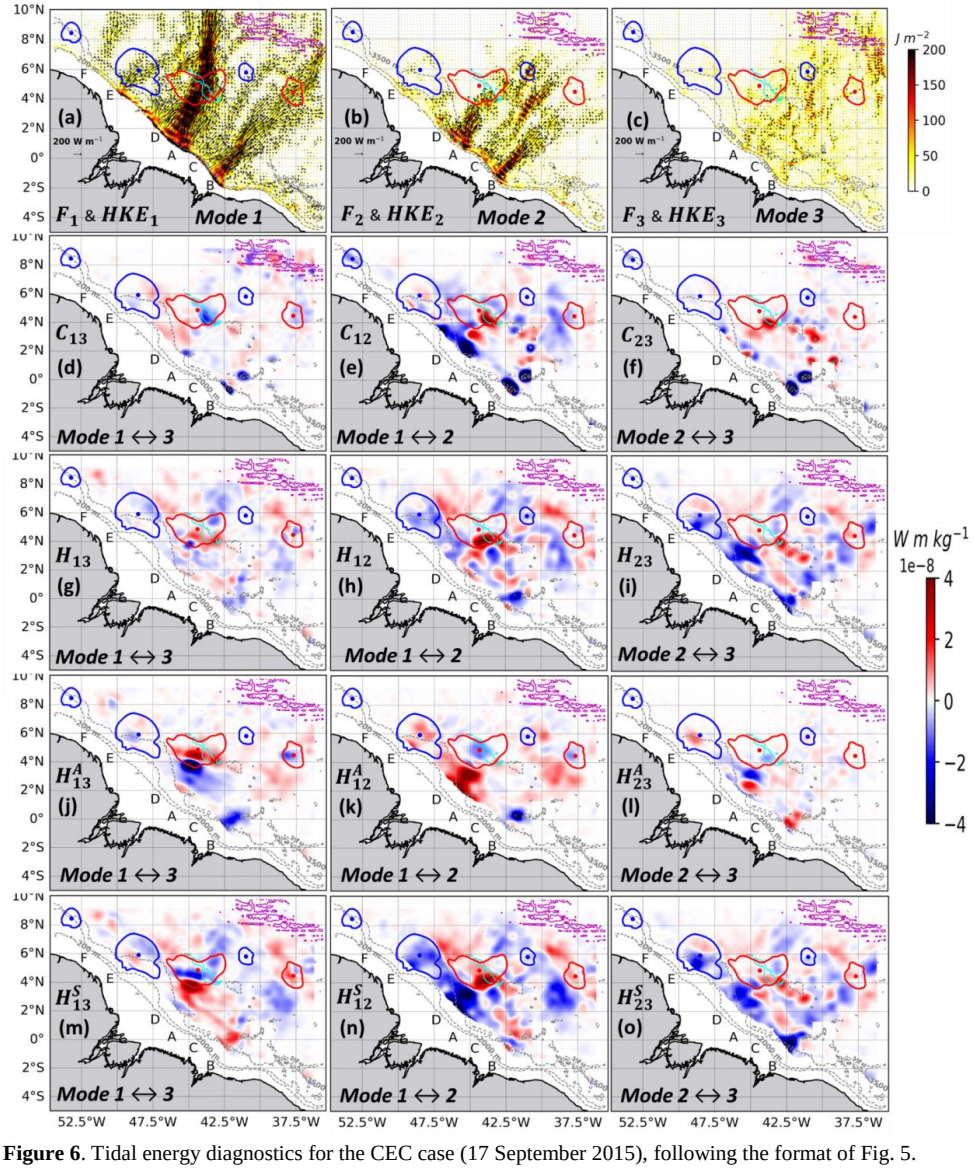

Figure 6. Tidal energy diagnostics for the CEC case (17 September 2015), following the format of Fig. 5.

3.2.3 CEE Case: IT Encountering a CE Edge

Finally, we assess IT interactions with the periphery of a surface-intensified CE centered at 5.3° N, 45.0° W (radius 143 km, maximum velocity 1.23 m s^{-1}, core bounded by 23–25.5 kg m^{-3} isopycnals extending ~100 m above the pycnocline).

This interaction yields a different kinematic response. The incident Mode-1 energy fluxes from sites A and D converge and, at the eddy edge, clearly diffract into two distinct beams (Fig. 7a): one propagating northward

https://doi.org/10.5194/egusphere-2025-6390
Preprint. Discussion started: 30 December 2025

(~39°) and the other eastward (~35°) relative to their northeastward incident direction. The northward-refracted beam maintains high HKE (150–200 J m^{-2}), while HKE is sharply reduced (25–50 J m^{-2}) in the northeast lee of the CE (Fig. 7a). Separately, the eastward-refracted beam, less energetic (HKE <100 J m^{-2}) than the northward beam, passes near the eastern periphery of a small AE. Mode-2 flux is sheared at the CE periphery with limited directional change (Fig. 7b), and Mode-3 becomes trapped along the northeastern CE edge and near the ridge (Fig. 7c). Consistent with previous cases, Mode-1 and Mode-2 exhibit higher energy flux amplitudes (>200 W m^{-1}) than Mode-3 (<200 W m^{-1}), and the energy flux patterns is supported by the vertical structures of the baroclinic velocity (Appendix A, Figs. A1, A4).

As in prior cases, the analysis identified topographic scattering (C_{mn}) and horizontal shear (H_{mn}) of the background flow as the two dominant mechanisms driving intermodal scattering in the CEE case.

The analysis of the term Cmn reveals a pattern modulated by the CE edge and seamount along the IT path from sites A and D. A dominant forward energy transfer ($|C_{mn}| \sim 4 \times 10^{-8}$ W m kg^{-1}) from Mode-1 to Mode-2 (Figs. 7e, blue patches) and from Mode-1 to Mode-3 IT (Figs. 7d, blue patches) occurs near the shelf break. Near the eastern edge of the CE and the southern flank of the seamount, a backward energy transfer occurs between IT modes (except between Mode-1 and Mode-3). Specifically, energy is gained by Mode-1 from Mode-2 IT (Figs. 7e, red patches) and by Mode-2 from Mode-3 IT (Figs. 7f, red patches), while energy is directly lost from Mode-1 to Mode-3 (Fig. 7d, blue patches). However, immediately after the seamount on the eastern CE edge, energy cascades forward from Mode-1 to Mode-2 (Fig. 7e, blue patches) and from Mode-2 to Mode-3 (Fig. 7f, blue patches). These overall patterns indicate that the CE edge inhibits the forward energy cascade observed in the NE case and instead initiates a dual mechanism: a potential flow shear-induced energy transfer from the background flow to IT modes, and a topographically-driven direct forward energy scattering between IT modes.

As in previous cases, the horizontal shear term (H_{mn}) in the CEE case is of comparable magnitude ($|H_{mn}| \sim 4 \times 10^{-8}$ W m^{-1} kg^{-1}) to the topographic scattering term. The net effect of H_{mn} (Figs. 7g-i) is primarily dominated by its symmetric part (Figs. 7m-o), facilitating energy exchange from the background flow to the IT modes along the IT path from sites A and D. Between the continental slope and the southern CE edge, energy is lost and gained between the Mode-1 background flow and Mode-2 IT (Figs. 7n, blue and red patches), and Mode-2 background flow and Mode-3 IT (Figs. 7o, blue and red patches). Near the eastern CE edge and the southern seamount flank, energy is gained by the Mode-1 background flow from the Mode-2 IT (Figs. 7n, red patches), and by the Mode-2 background flow from the Mode-3 IT (Figs. 7o, red patches). However, between Modes 1 and 3, the antisymmetric part of Hmn dominates (Figs. 7g,j), indicating an energy transfer between IT modes, where Mode-1 IT gains energy from Mode-3 IT (Figs. 7j, red patches near the CE edge and seamount). As in the CEC case, these patterns provide strong evidence for a dominant energy pathway from the background flow to the IT modes driven by horizontal shear, coupled with a topographically-driven direct forward energy transfer between IT modes.

In summary, in the CEE case, upon interacting with the CE periphery, each IT mode meets a distinct fate. Mode-1 IT from sites A and D splits into two energetic beams, propagating northward and eastward with energy fluxes exceeding 200 W m^{-1}. In contrast, Mode-2 IT is sheared apart, while Mode-3 IT is scattered by the eddy edge and

https://doi.org/10.5194/egusphere-2025-6390
Preprint. Discussion started: 30 December 2025

seafloor topography, its energy flux remaining below 200 W m^{-1}. During this encounter, a significant energy transfer (~10^{-8} W m kg^{-1}) occurs through a similar interplay as in the CEC case: 1) a dominant inverse energy cascade from the background flow to the IT modes (Mode-3 → Mode-2 → Mode-1) driven by horizontal shear, which can act to suppress the topographically-driven downscale energy, and 2) a direct forward energy transfer from Mode-1 to Mode-3 IT driven by topographic scattering.

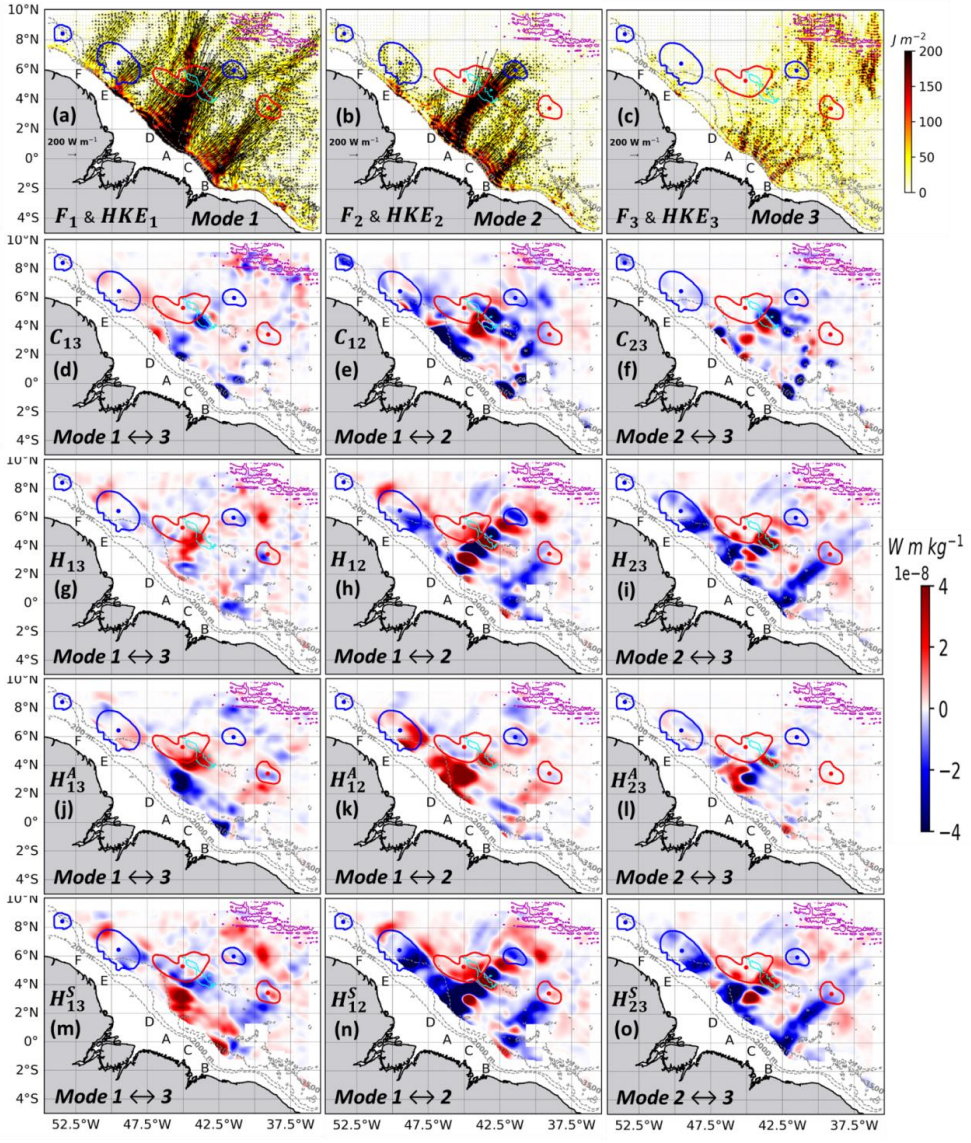

Figure 7. Tidal energy diagnostics for the CEE case (29 September 2015), following the format of Fig. 5.

https://doi.org/10.5194/egusphere-2025-6390
Preprint. Discussion started: 30 December 2025

4 Discussion

This study investigated the fate of M_2 IT energy on the Amazon shelf during the turbulent period of SOND 2015. We addressed three questions: (1) Does the IT propagate freely, deviate, or become trapped by mesoscale features? (2) Do these outcomes depend on the IT's vertical mode or the properties and location of the MEs (CE core vs. periphery)? (3) What are the synergistic roles of topography and CEs in governing modal energy transfers? By projecting energy flux into vertical modes and performing intermodal energy transfer terms, we dissected these interactions more deeply.

4.1 The Variable Fate of Internal Tides: Free Propagation, Deviation, and Trapping

Our results show that the fate of IT energy is not uniform but is dictated by interactions with mesoscale features, affecting the intensity and distribution of energy flux. The NE case established a baseline of efficient, long-range propagation, where the Mode-1 energy flux maintained amplitudes exceeding 200 W m^{-1} along a coherent beam for over 1100 km. This free propagation aligns with previous studies (e.g., Xu et al., 2016; Fan et al., 2024) and confirms Mode-1's characteristic as a freely propagating IT (Zhao et al., 2010). Its path is governed by Snell's law (Small, 2001; Zhao, 2014), with minimal Coriolis constraint (f) near the equator ($f/\omega_{M2} << 1$, with ω_{M2} the M_2 tidal frequency), shifting steering mechanisms to wave–current and wave–stratification interactions. The stability of the Mode-1 IT beam in background flow is consistent with ray-tracing results, such as those at the Hawaiian Ridge, where typical currents had only slight effects (Rainville and Pinkel, 2006). While high-resolution and idealized simulations suggested reduced Coriolis constraints at low latitudes (Wang et al., 2021; Le Dizes et al., 2025), our realistic simulations advance these findings by forcing nonlinear interactions in a highly complex field.

In the NE case, strong background flow, particularly the NECC, moved quasi-perpendicular to incident Mode-1 IT beams, and horizontal stratification varied. The subcritical seamount ($h_{max}/H \sim 0.2$) acted only as a minor directional obstacle ($\lambda_1/w_{max} \sim 0.9–1.25$) for propagating Mode-1 IT, though it could affect higher-order modes intensified near the bottom.

The presence of a CE consistently disrupted free propagation, leading to deviation or trapping with distinct energy modulations. The incident Mode-1 IT was deviated into convergent energy beams, creating a zone of reduced energy flux in the lee of the eddy, consistent with processes modeled by Wang and Legg (2023) and Dunphy and Lamb (2014). This reduction in coherent energy flux is strongly supported by in situ observations south of the Azores, which reported a reduction in low-mode IT energy flux during interactions with a surface-intensified eddy (Löb et al., 2020). Across all cases, Mode-3 energy never formed a coherent beam and consistently exhibited the weakest fluxes (<200 W m^{-1}). The most relevant blockage occurred for Mode-2 (with flux amplitude comparable to Mode-1) in the CEC case, where an otherwise energetic mode was completely impeded at the eddy–seamount interface. This vulnerability aligns with global observations that Mode-2 M_2 IT generally has smaller sea surface height amplitudes and shorter propagation distances (O[100 km]) than Mode-1 (Zhao, 2018). MEs thus act as potent filters that selectively dissipate or trap the energy of specific vertical modes.

4.2 The Dual Control of IT Response: Vertical Mode and Eddy Encounters

https://doi.org/10.5194/egusphere-2025-6390
Preprint. Discussion started: 30 December 2025

A key finding of this study is that the IT responses to an ME is dually controlled by its vertical mode and the specific properties and location of the eddy encounter. Mode-1 IT is robust and long-ranging but susceptible to beam steering, while Mode-2 is far more vulnerable to damping and blocking. Mode-3 IT is consistently weak and scattered, behaving as a trapped mode that seldom forms coherent beams. Only Mode-1 IT underwent large-scale deviation by MEs or background flow fields, with energy loss occurring via forward energy transfer at localized, energetic interaction sites (seamount, eddy boundaries). This is consistent with studies showing that remote IT energy is scattered to higher modes at continental margins (Siyanbola et al., 2024; Fan et al., 2024) and with findings that an ME focuses Mode-1 energy flux in specific areas while inducing vertical mode scattering (Dunphy and Lamb, 2014). Our observation of Mode-1 deviation is analogous to the redirection of ISWs by ME fields (Liao et al., 2012; Goret et al., 2025).

IT beam deviation is sensitive to eddy properties. The direction of deviation depends strongly on eddy polarity, as shown by previous studies (e.g., Huang et al., 2018; Guo et al., 2023; Dunphy et al., 2017; Wang and Legg, 2023; Li et al., 2024) and as observed—though not focused in our study—in the energy flux path emanating from the less energetic generation site E (see Section 3.1, Fig. 4b: deviation of the energy flux due to an AE core centered at 5.9°N and 48.5°W). While earlier work noted that AE cores speed up Mode-1 propagation and induce clockwise (southward) refraction, whereas CE cores slow it down and induce counterclockwise (northward) refraction, our findings link specific interaction geometries to distinct intermodal energy pathways in a realistic framework.

The distinction between the CEC (core) and CEE (periphery) cases reveals that the same CE can impose fundamentally different fates on a passing Mode-1 IT. Interaction with the eddy core refracted the incident beam coherently by ~35° into a single northward path. In contrast, an encounter at the eddy periphery diffracted the energy into two distinct beams propagating northward (~39°) and eastward (~35°). This demonstrates that “eddy lensing” is nuanced and sensitive to the radial structure and shear fields of the eddy. Recent SWOT satellite observations corroborate this finding, documenting analogous refraction at a CE core and diffraction at a western AE edge within the study region (Goret et al., 2025). Our results provide a mechanistic explanation for incoherent IT signals and variable trapping noted in high-resolution models of the ASOND period in this region (Tchilibou et al., 2022).

While Mode-1 IT is susceptible to beam steering, higher modes (Mode-2 and Mode-3) are more sensitive to topography and are quickly damped, trapped, and become primary recipients of energy via downscale cascades linked to topographic scattering (Lahaye et al., 2020; Fan et al., 2024; Bella et al., 2024). Our results advance these findings by showing that higher modes are also more sensitive to the presence of a CE in conjunction with a localized seamount. Therefore, the energy scattering from lower to higher IT modes and the trapping of those modes by CE’s flow are two linked processes facilitating the IT dissipation (Wang and Legg, 2023).

This study was limited to surface-intensified eddies. Future work should investigate whether similar IT interactions occur with other ME types, such as deep intrathermocline eddies or complex multi-eddy systems. A

https://doi.org/10.5194/egusphere-2025-6390
Preprint. Discussion started: 30 December 2025

key question is whether eddies with thin vertical structures—and thus higher vertical modes—are capable of trapping ITs, which warrants specific examination.

4.3 Synergistic Roles of Topography, Background Flow, and CEs in Modal Energy Transfers

Our results reveal a complex hierarchy of interactions that governs modal energy transfers, where even without strong MEs, the combined effects of topography and background flow establish a baseline for energy pathways.

The NE case shows the seamount acts as a critical site for modal scattering, driving a dominant forward energy cascade from Mode-1 to Mode-2 to Mode-3 IT (~4×10^{-8} W m kg^{-1}). This magnitude of transfer is characteristic of interactions over abrupt topography, consistent with quantifications of energy cascades on continental slopes (Kelly and Nash, 2012). This topographically driven transfer is significantly modulated by background flow (NECC/NBC) through horizontal shear mechanisms of comparable strength, aligning with studies in the North Atlantic concluding that low-frequency flow strongly impacts the IT energy cycle, often transferring energy toward smaller scales (Bella et al., 2024). Background flow actively participates in energy exchange, facilitating transfer from Mode-3 background flow to Mode-2 IT over the seamount. Thus, seamount–topography interaction with background flow creates a dynamic environment for energy redistribution even before considering ME effects.

Introducing a CE—particularly one co-located with the seamount, as in the CEC case—fundamentally reorganizes the energy transfer landscape. The CE's strong horizontal shear dominates background flow effects and reverses the canonical energy pathway, initiating a dominant inverse energy cascade from background flow to IT modes. This shift from the topographically driven forward cascade observed in the NE case is mediated by horizontal shear, supported by analyses using coupled-mode shallow-water models that emphasize advection terms involving mean flow and buoyancy shear (Kelly et al., 2016). The synergy between the CE and seamount creates competing pathways: topographically driven forward scattering operates concurrently with eddy-driven inverse cascades, leading to complex energy redistribution that explains observed modal blocking and trapping. This aligns with studies detailing how CEs and AEs differently affect topographic scattering (Li et al., 2024) and underscores that cross-scale energy exchange is a key driver in the tropical western Atlantic (Wang et al., 2025).

The consistent co-location of CEs and the seamount with background flow (e.g., NECC) suggests background flow variability further enhances IT refraction and diffraction—a mechanism supported by studies in other western boundary currents (Duda et al., 2018; Cao et al., 2022; Xu et al., 2021; Kelly and Lermusiaux, 2016; Chen et al., 2022; Pereira et al., 2007; Kelly et al., 2016), though fully isolating the NECC's individual contribution will require future idealized modeling.

5 Conclusion

This study illustrates the complex pathways of M_2 IT energy in the region off the Amazon shelf during the period of SOND 2015. By applying vertical mode decomposition to high-resolution NEMO-AMAZON36 simulations, we examined three representative interaction cases (Fig. 8): undisturbed propagation until crossing a topography,

https://doi.org/10.5194/egusphere-2025-6390
Preprint. Discussion started: 30 December 2025

interaction with a CE core, and interaction with a CE eastern periphery. For each case, we systematically computed the intermodal energy transfer terms to identify the governing mechanisms.

The two primary conclusions are as follows:

First, the specific response of an IT—whether it propagates freely or deviates—is dually controlled by its vertical modal structure and the properties of the mesoscale eddy it encounters. In the absence of a strong eddy (NE case), Mode-1 IT propagated freely as a coherent, long-range beam. Interactions with a CE, however, consistently disrupted this pattern, leading to refraction, diffraction, or trapping. An encounter with a CE core coherently refracted the Mode-1 beam northward by approximately 35°, maintaining high energy fluxes (>200 W m^{-1}). In contrast, interaction at the eddy periphery diffracted the energy, splitting it into two distinct beams propagating northward (~39°) and eastward (~35°). Higher modes were particularly susceptible to trapping; Mode-2 energy flux—despite an amplitude comparable to Mode-1—was completely blocked and trapped at the eddy-seamount interface, while Mode-3 energy remained weak (<200 W m^{-1}), scattered, and confined near the generation site without ever forming a coherent beam.

Second, the redistribution of energy via intermodal transfers is governed by a hierarchy of synergistic interactions between the seamount and the background flow of the eddy. In the NE case, the seamount drives a dominant forward energy cascade from Mode-1 to higher modes (O (10^{-8} W m kg^{-1})), a process modulated by the background flow's horizontal shear. The presence of a CE colocated with the seamount fundamentally reorganizes this dynamic. The CE's strong horizontal shear initiates a dominant inverse energy cascade from the background flow to the IT modes, directly competing with the ongoing topographic forward cascade. This specific synergy is crucial for explaining the extreme blocking of Mode-2 and the complex redistribution of energy fluxes observed.

Nonetheless, the region is shaped by a complex, co-located interplay of forces—including the NECC, MEs (CEs and AEs), and the topographic features—making it challenging to fully isolate their individual effects on ITs in realistic simulations. To disentangle and quantify the specific contributions of each mechanism with greater precision, future work should employ idealized modeling frameworks. Such an approach is essential for isolating the deterministic impacts of mesoscale flow and advancing toward a predictive understanding of IT energy pathways in complex oceanic environments.

https://doi.org/10.5194/egusphere-2025-6390
Preprint. Discussion started: 30 December 2025

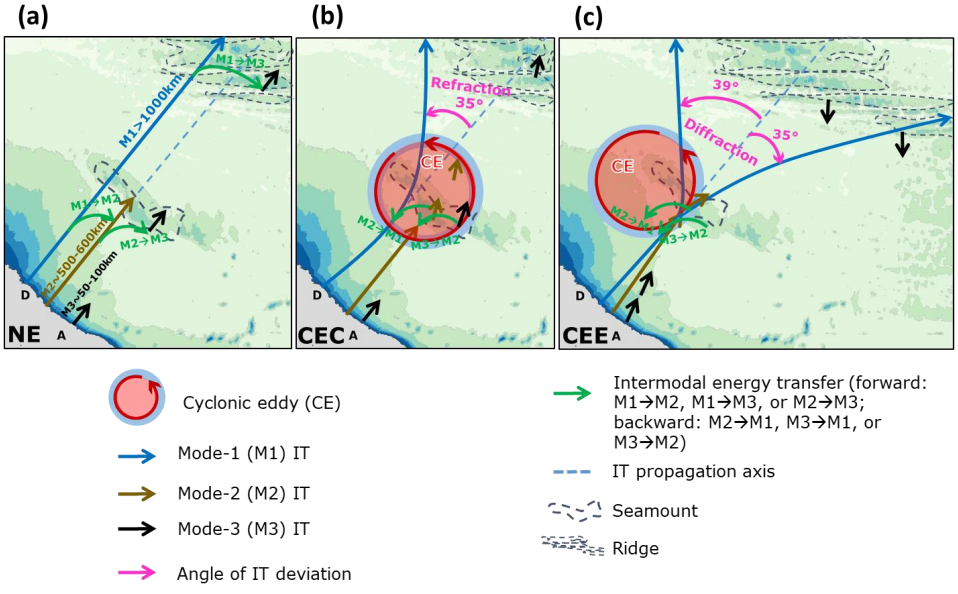

Figure 8. Schematics summarizing the fate of propagating M2 IT from generation sites A and D on the Amazon shelf-break. The panels correspond to the three analyzed cases: (a) NE, (b) CEC, and (c) CEE. The diagram highlights the key dynamic IT responses—inter-modal scattering, refraction, and diffraction—resulting from interaction with mesoscale structures, emphasizing the pronounced effects of CEs. The specific IT response is dually controlled by its vertical mode and the CE encounter properties. Furthermore, intermodal energy scattering is governed by a hierarchical synergy between the seamount and the CE's background flow.

Data availability

The NEMOv3.6 model outputs are available upon request by contacting the corresponding author.

Authors contributions

Funding acquisition: AKL, XC and MA. Conceptualization and methodology: FK, AKL and XC. Data processing: FK. Formal analysis: FK with interactions from all co-authors. Preparation and writing of the manuscript: FK with contributions from all co-authors.

Competing interests

The contact author has declared that none of the authors has any competing interests.

Acknowledgments

This work is a contribution to the project "MIAMAZ-ETI" (Multi-Sensors study of the fine scale processes and their impacts on ocean color, off the Amazon shelf : Eddy-Tides Interactions). The authors thank Guillaume Morvan for providing NEMO model data.

Financial support

https://doi.org/10.5194/egusphere-2025-6390
Preprint. Discussion started: 30 December 2025

This work is part of the PhD thesis of Fabius Kouogang, conducted under the joint supervision of Ariane Koch-Larrouy, Xavier Carton, and Moacyr Araujo. The research received support from “Coordenação de Aperfeiçoamento de Pessoal de Nível Superior” (CAPES); the Institute of Research for Development (IRD, France) via an ARTS grant; the ISblue project, Interdisciplinary graduate school for the blue planet (ANR-17-EURE-0015) and co-funded by a grant from the French government under the program "Investissements d'Avenir" embedded in France 2030; and the "Centre National d’Études Spatiales" (CNES) through the APR MIAMAZ-ETI project (Principal Investigators: Ariane Koch-Larrouy, Camila Artana, Isabelle Dadou). Moacyr Araujo was funded by the Brazilian National Council for Scientific and Technological Development (CNPq), and Xavier Carton received support from the University of Western Brittany.

References

Aguedjou, H. M. A., Dadou, I., Chaigneau, A., Morel, Y., and Alory, G.: Eddies in the tropical Atlantic Ocean and their seasonal variability, Geophys. Res. Lett., 46, 12156–12164, https://doi.org/10.1029/2019GL083925, 2019.

Aguedjou, H. M. A., Chaigneau, A., Dadou, I., Morel, Y., Pegliasco, C., Da-Allada, C. Y., and Baloïtcha, E.: What can we learn from observed temperature and salinity isopycnal anomalies at eddy generation sites? Application in the tropical Atlantic Ocean, J. Geophys. Res.: Oceans, 126, e2021JC017630, https://doi.org/10.1029/2021JC017630, 2021.

Alford, M. H., Simmons, H. L., Marques, O. B., and Girton, J. B.: Internal tide attenuation in the North Pacific, Geophys. Res. Lett., 46, 8205–8213, https://doi.org/10.1029/2019GL082648, 2019.

Alford, M. H., and Zhao, Z.: Global patterns of low-mode internal-wave propagation. Part I: Energy and energy flux, J. Phys. Oceanogr., 37, 1829–1848, https://doi.org/10.1175/jpo3085.1, 2007.

Assene, F., Koch-Larrouy, A., Dadou, I., Tchilibou, M., Morvan, G., Chanut, J., Costa Da Silva, A., Vantrepotte, V., Allain, D., and Tran, T.-K.: Internal tides off the Amazon shelf – Part 1: The importance of the structuring of ocean temperature during two contrasted seasons, Ocean Sci., 20, 43–67, https://doi.org/10.5194/os-20-43-2024, 2024.

Barbot, S., Lyard, F., Tchilibou, M., and Carrere, L.: Background stratification impacts on internal tide generation and abyssal propagation in the western equatorial Atlantic and the Bay of Biscay, Ocean Sci., 17, 1563–1583, https://doi.org/10.5194/os-17-1563-2021, 2021.

Barnier, B., Reynaud, T., Beckmann, A., Böning, C., Molines, J.-M., Barnard, S., and Jia, Y.: On the seasonal variability and eddies in the North Brazil Current: Insights from model intercomparison experiments, Prog. Oceanogr., 48, 195–230, https://doi.org/10.1016/S0079-6611(01)00005-2, 2001.

https://doi.org/10.5194/egusphere-2025-6390
Preprint. Discussion started: 30 December 2025

Bella, A., Lahaye, N., and Tissot, G.: Internal tide energy transfers induced by mesoscale circulation and topography across the North Atlantic, J. Geophys. Res.: Oceans, 129, e2024JC020914, https://doi.org/10.1029/2024JC020914, 2024.

Brandt, P., Rubino, A., and Fischer, J.: Large-amplitude internal solitary waves in the North Equatorial Countercurrent, J. Phys. Oceanogr., 32, 1567–1573, https://doi.org/10.1175/1520-0485(2002)032<1567:LAISWI>2.0.CO;2, 2002.

Buijsman, M. C., Legg, S., and Klymak, J.: Double-ridge internal tide interference and its effect on dissipation in Luzon Strait, J. Phys. Oceanogr., 42, 1337–1356, https://doi.org/10.1175/jpo-d-11-0210.1, 2012.

Cao, A., Guo, Z., Wang, S., Guo, X., and Song, J.: Incoherence of the M2 and K1 internal tides radiated from the Luzon Strait under the influence of looping and leaping Kuroshio, Prog. Oceanogr., 206, 102850, https://doi.org/10.1016/j.pocean.2022.102850, 2022.

Chen, J., Zhu, X.-H., Wang, M., Zheng, H., Zhao, R., Nakamura, H., and Yamashiro, T.: Incoherent signatures of internal tides in the Tokara Strait modulated by the Kuroshio, Prog. Oceanogr., 206, 102863, https://doi.org/10.1016/j.pocean.2022.102863, 2022.

Clément, L., Frajka-Williams, E., Sheen, K. L., Brearley, J. A., and Garabato, A. N.: Generation of internal waves by eddies impinging on the western boundary of the North Atlantic, J. Phys. Oceanogr., 46, 1067–1079, https://doi.org/10.1175/JPO-D-14-0241.1, 2016.

De Macedo, C. R., Koch-Larrouy, A., Da Silva, J. C. B., Magalhães, J. M., Lentini, C. A. D., Tran, T. K., Rosa, M. C. B., and Vantrepotte, V.: Spatial and temporal variability of mode-1 and mode-2 internal solitary waves from MODIS/TERRA sunglint off the Amazon shelf, Ocean Sci., 19, 1357–1374, https://doi.org/10.5194/os-19-1357-2023, 2023.

Delpech, A., Cravatte, S., Marin, F., Morel, Y., Gronchi, E., and Kestenare, E.: Observed tracer fields structuration by middepth zonal jets in the tropical Pacific, J. Phys. Oceanogr., 50, 281–304, https://doi.org/10.1175/JPO-D-19-0091.1, 2020.

Didden, N., and Schott, F.: Eddies in the North Brazil Current retroflection region observed by Geosat altimetry, J. Geophys. Res., 98, 20121, https://doi.org/10.1029/93JC01184, 1993.

Duda, T. F., Lin, Y.-T., Buijsman, M., and Newhall, A. E.: Internal tidal modal ray refraction and energy ducting in baroclinic Gulf Stream currents, J. Phys. Oceanogr., 48, 1965–1983, https://doi.org/10.1175/JPO-D-17-0230.1, 2018.

https://doi.org/10.5194/egusphere-2025-6390
Preprint. Discussion started: 30 December 2025

Dunphy, M., and Lamb, K. G.: Focusing and vertical mode scattering of the first mode internal tide by mesoscale eddy interaction, J. Geophys. Res.: Oceans, 119, 523–536, https://doi.org/10.1002/2013JC009363, 2014.

Dunphy, M., Ponte, A. L., Klein, P., and Le Gentil, S.: Low-mode internal tide propagation in a turbulent eddy field, J. Phys. Oceanogr., 47, 649–665, https://doi.org/10.1175/JPO-D-16-0099.1, 2017.

Ernst, P. A., Subrahmanyam, B., Morel, Y., Trott, C. B., and Chaigneau, A.: Subsurface eddy detection optimized with potential vorticity from models in the Arabian Sea, J. Atmos. Ocean. Technol., 40, 677–700, https://doi.org/10.1175/JTECH-D-22-0050.1, 2023.

Ertel, H.: On hydrodynamic eddy theorems, Phys. Z., 43, 526–529, 1942.

Fan, L., Sun, H., Yang, Q., and Li, J.: Numerical investigation of interaction between anticyclonic eddy and semidiurnal internal tide in the northeastern South China Sea, Ocean Sci., 20, 241–264, https://doi.org/10.5194/os-20-241-2024, 2024.

Fassoni-Andrade, A. C., Durand, F., Azevedo, A., Bertin, X., Santos, L. G., Khan, J. U., Testut, L., and Moreira, D. M.: Seasonal to interannual variability of the tide in the Amazon estuary, Cont. Shelf Res., 255, 104945, https://doi.org/10.1016/j.csr.2023.104945, 2023.

Fratantoni, D. M., and Glickson, D. A.: North Brazil Current Ring generation and evolution observed with SeaWiFS, J. Phys. Oceanogr., 32, 1058–1074, https://doi.org/10.1175/1520-0485(2002)032<1058:NBCRGA>2.0.CO;2, 2002.

Garrett, C., and Kunze, E.: Internal tide generation in the deep ocean, Annu. Rev. Fluid Mech., 39, 57–87, https://doi.org/10.1146/ANNUREV.FLUID.39.050905.110227, 2007.

GEBCO Compilation Group: GEBCO_2020 grid, British Oceanographic Data Centre, National Oceanography Centre, NERC, UK [data set], https://doi.org/10.5285/a29c5465-b138-234d-e053-6c86abc040b9, 2020.

Gerkema, T., and Zimmerman, J. T. F.: An introduction to internal waves, Lecture Notes, Royal Netherlands Institute for Sea Research, 2008.

Goret, C., Koch-Larrouy, A., Kouogang, F., de Macedo, C. R., M'Hamdi, A., Magalhães, J., da Silva, J. C. B., Tchilibou, M., Artana, C., Dadou, I., Delepoulle, A., Barbot, S., Ballarotta, M., Carrère, L., and Costa da Silva, A.: Internal solitary waves refraction and diffraction from interaction with eddies off the Amazon shelf from SWOT, EGUsphere [preprint], https://doi.org/10.5194/egusphere-2025-3933, 2025.

Guo, Z., Wang, S., Cao, A., Xie, J., Song, J., and Guo, X.: Refraction of the M2 internal tides by mesoscale eddies in the South China Sea, Deep-Sea Res. Pt. I, 192, 103946, https://doi.org/10.1016/j.dsr.2022.103946, 2023.

https://doi.org/10.5194/egusphere-2025-6390
Preprint. Discussion started: 30 December 2025

Hersbach, H., Bell, B., Berrisford, P., Hirahara, S., Horányi, A., Muñoz-Sabater, J., Nicolas, J., Peubey, C., Radu, R., Schepers, D., Simmons, A., Soci, C., Abdalla, S., Abellan, X., Balsamo, G., Bechtold, P., Biavati, G., Bidlot, J., Bonavita, M., De Chiara, G., Dahlgren, P., Dee, D., Diamantakis, M., Dragani, R., Flemming, J., Forbes, R., Fuentes, M., Geer, A., Haimberger, L., Healy, S., Hogan, R. J., Hólm, E., Janisková, M., Keeley, S., Laloyaux, P., Lopez, P., Lupu, C., Radnoti, G., de Rosnay, P., Rozum, I., Vamborg, F., Villaume, S., and Thépaut, J.-N.: The ERA5 global reanalysis, Q. J. Roy. Meteor. Soc., 146, 1999–2049, https://doi.org/10.1002/qj.3803, 2020.

Huang, X., Wang, Z., Zhang, Z., Yang, Y., Zhou, C., Yang, Q., Zhao, W., and Tian, J.: Role of mesoscale eddies in modulating the semidiurnal internal tide: Observation results in the northern South China Sea, J. Phys. Oceanogr., 48, 1749–1768, https://doi.org/10.1175/JPO-D-17-0238.1, 2018.

Johnston, T. M. S., and Merrifield, M. A.: Internal tide scattering at the Line Islands Ridge, J. Geophys. Res., 108, 3365, https://doi.org/10.1029/2003JC001844, 2003.

Kelly, S. M.: The vertical mode decomposition of surface and internal tides in the presence of a free surface and arbitrary topography, J. Phys. Oceanogr., 46, 3845–3859, https://doi.org/10.1175/JPO-D-16-0164.1, 2016.

Kelly, S. M., and Lermusiaux, P. F. J.: The cascade of tidal energy from low to high modes on a continental slope, J. Phys. Oceanogr., 42, 1276–1292, https://doi.org/10.1175/JPO-D-11-0231.1, 2012.

Kelly, S. M., and Lermusiaux, P. F. J.: Internal-tide interactions with the Gulf Stream and Middle Atlantic Bight shelfbreak front, J. Geophys. Res.: Oceans, 121, 6271–6294, https://doi.org/10.1002/2016JC011986, 2016.

Kelly, S. M., Lermusiaux, P. F. J., and Duda, T. F.: A coupled-mode shallow-water model for tidal analysis: Internal tide reflection and refraction by the Gulf Stream, J. Phys. Oceanogr., 46, 3747–3767, https://doi.org/10.1175/JPO-D-16-0125.1, 2016.

Kelly, S. M., Nash, J. D., Martini, K. I., Alford, M. H., and Kunze, E.: The cascade of tidal energy from low to high modes on a continental slope, J. Phys. Oceanogr., 42, 1217–1232, https://doi.org/10.1175/jpo-d-11-0231.1, 2012.

Kelly, S. M., Nash, J. D., and Kunze, E.: Internal-tide energy over topography, J. Geophys. Res.-Oceans, 115, C06014, https://doi.org/10.1029/2009JC005618, 2010.

Kelly, S. M., and Nash, J. D.: Internal-tide generation and destruction by shoaling internal tides, Geophys. Res. Lett., 37, L23611, https://doi.org/10.1029/2010GL045598, 2010.

Kerry, C. G., Powell, B. S., and Carter, G. S.: Effects of remote generation sites on model estimates of M2 internal tides in the Philippine Sea, J. Phys. Oceanogr., 43, 187–204, https://doi.org/10.1175/jpo-d-12-081.1, 2013.

https://doi.org/10.5194/egusphere-2025-6390
Preprint. Discussion started: 30 December 2025

Koch-Larrouy, A., Atmadipoera, A., van Beek, P., Madec, G., Aucan, J., Lyard, F., Grelet, J., and Souhaut, M.: Estimates of tidal mixing in the Indonesian archipelago from multidisciplinary INDOMIX in-situ data, Deep-Sea Res. Pt. I, 106, 136–153, https://doi.org/10.1016/j.dsr.2015.09.007, 2015.

Kouogang, F., Koch-Larrouy, A., Magalhaes, J., Costa Da Silva, A., Kerhervé, D., Bertrand, A., Cervelli, E., Ternon, J.-F., Rousselot, P., Lee, J., Rollnic, M., and Araujo, M.: Turbulent dissipation from AMAZOMIX off the Amazon shelf along internal tide paths, Ocean Sci., 21, 1589–1608, https://doi.org/10.5194/os-21-1589-2025, 2025.

Kunze, E.: Internal-wave-driven mixing: Global geography and budgets, J. Phys. Oceanogr., 47, 1325–1345, https://doi.org/10.1175/JPO-D-16-0141.1, 2017.

Kurian, J., Colas, F., Capet, X., McWilliams, J. C., and Chelton, D. B.: Eddy properties in the California Current System, J. Geophys. Res.-Oceans, 116, https://doi.org/10.1029/2010jc006895, 2011.

Lahaye, N., Gula, J., and Roullet, G.: Internal tide cycle and topographic scattering over the north mid-Atlantic ridge, J. Geophys. Res.: Oceans, 125, e2020JC016376, https://doi.org/10.1029/2020JC016376, 2020.

Lahaye, N., Ponte, A., Le Sommer, J., and Albert, A.: Internal tide surface signature and incoherence in the North Atlantic, Geophys. Res. Lett., 51, e2024GL108508, https://doi.org/10.1029/2024GL108508, 2024.

Le Dizes, C., Grisouard, N., Thual, O., and Mercier, M. J.: Three-dimensional modelling of internal tide generation over isolated seamounts in a rotating ocean, J. Fluid Mech., 1022, A5, https://doi.org/10.1017/jfm.2025.10647, 2025.

Lellouche, J.-M., Greiner, E., Le Galloudec, O., Garric, G., Regnier, C., Drevillon, M., Benkiran, M., Testut, C.-E., BourdalleBadie, R., Gasparin, F., Hernandez, O., Levier, B., Drillet, Y., Remy, E., and Le Traon, P.-Y.: Recent updates to the Copernicus Marine Service global ocean monitoring and forecasting realtime 1=12◦ high-resolution system, Ocean Sci., 14, 1093–1126, https://doi.org/10.5194/os-14-1093-2018, 2018.

Li, B., Xu, M., Chen, W., Yuan, Y., Liu, Y., and Li, S.: Evolution of internal tide scattering hidden below mesoscale eddies, Prog. Oceanogr., 226, 103305, https://doi.org/10.1016/j.pocean.2024.103305, 2024.

Liao, G., Yang, C., Xu, X., Shi, X., Yuan, Y., and Huang, W.: Effects of mesoscale eddies on the internal solitary wave propagation, Acta Oceanol. Sin., 31, 26–40, https://doi.org/10.1007/s13131-012-0205-5, 2012.

Lorenz, E. N.: Available potential energy and the maintenance of the general circulation, Tellus, 7, 157–167, https://doi.org/10.1111/j.2153-3490.1955.tb01148.x, 1955.

https://doi.org/10.5194/egusphere-2025-6390
Preprint. Discussion started: 30 December 2025

Löb, J., Köhler, J., Mertens, C., Walter, M., Li, Z., and von Storch, J.-S.: Observations of the low-mode internal tide and its interaction with mesoscale flow south of the Azores, J. Geophys. Res.: Oceans, 125, e2019JC015879, https://doi.org/10.1029/2019JC015879, 2020.

Lyard, F. H., Allain, D. J., Cancet, M., Carrère, L., and Picot, N.: FES2014 global ocean tide atlas: Design and performance, Ocean Sci., 17, 615–649, https://doi.org/10.5194/os-17-615-2021, 2021.

Madec, G., Bourdallé-Badie, R., Chanut, J., Clementi, E., Coward, A., Ethé, C., Iovino, D., Lea, D., Lévy, C., Lovato, T., Martin, N., Masson, S., Mocavero, S., Rousset, C., Storkey, D., Vancoppenolle, M., Müeller, S., Nurser, G., Bell, M., and Samson, G.: NEMO ocean engine, Zenodo, https://doi.org/10.5281/zenodo.3878122, 2019.

Magalhaes, J. M., Da Silva, J. C. B., Buijsman, M. C., and Garcia, C. A. E.: Effect of the North Equatorial Counter Current on the generation and propagation of internal solitary waves off the Amazon shelf (SAR observations), Ocean Sci., 12, 243–255, https://doi.org/10.5194/os-12-243-2016, 2016.

Mathur, M., Carter, G. S., and Peacock, T.: Topographic scattering of the low-mode internal tide in the deep ocean, J. Geophys. Res.-Oceans, 119, 2165–2182, https://doi.org/10.1002/2013JC009152, 2014.

Morel, Y., Gula, J., and Ponte, A.: Potential vorticity diagnostics based on balances between volume integral and boundary conditions, Ocean Model., 138, 23–35, https://doi.org/10.1016/j.ocemod.2019.04.004, 2019.

Morel, Y., Morvan, G., Benshila, R., Renault, L., Gula, J., and Auclair, F.: An “objective” definition of potential vorticity: Generalized evolution equation and application to the study of coastal upwelling instability, Ocean Model., 186, 102287, https://doi.org/10.1016/j.ocemod.2023.102287, 2023.

Nakamura, N.: Modified Lagrangian-mean diagnostics of the stratospheric polar vortices. Part I. Formulation and analysis of GFDL SKYHI GCM, J. Atmos. Sci., 52, 2096–2108, https://doi.org/10.1175/1520-0469(1995)052<2096:MLMDOT>2.0.CO;2, 1995.

Nash, J. D., Kelly, S. M., Shroyer, E. L., Moum, J. N., and Duda, T. F.: The unpredictable nature of internal tides on continental shelves, J. Phys. Oceanogr., 42, 1981–2000, https://doi.org/10.1175/JPO-D-12-028.1, 2012.

Okubo, A.: Horizontal dispersion of floatable particles in vicinity of velocity singularities such as convergence, Deep-Sea Res., 17, 445, https://doi.org/10.1016/0011-7471(70)90059-8, 1970.

Pereira, A. F., Castro, B. M., Calado, L., and da Silveira, I. C. A.: Numerical simulation of M2 internal tides in the South Brazil Bight and their interaction with the Brazil Current, J. Geophys. Res., 112, C04009, https://doi.org/10.1029/2006JC003673, 2007.

https://doi.org/10.5194/egusphere-2025-6390
Preprint. Discussion started: 30 December 2025

Rainville, L., and Pinkel, R.: Propagation of low-mode internal waves through the ocean, J. Phys. Oceanogr., 36, 1220–1236, https://doi.org/10.1175/JPO2924.1, 2006.

Savage, A. C., Waterhouse, A. F., and Kelly, S. M.: Internal tide nonstationarity and wave–mesoscale interactions in the Tasman Sea, J. Phys. Oceanogr., 50, 2931–2951, https://doi.org/10.1175/JPO-D-20-0081.1, 2020.

Silva, A. C., Bourles, B., and Araujo, M.: Circulation of the thermocline salinity maximum waters off the Northern Brazil as inferred from in situ measurements and numerical results, Ann. Geophys., 27, 1861–1873, https://doi.org/10.5194/angeo-27-1861-2009, 2009.

Siyanbola, O. Q., Buijsman, M. C., Delpech, A., Barkan, R., Pan, Y., and Arbic, B. K.: Interactions of remotely generated internal tides with the U.S. West Coast continental margin, J. Geophys. Res.: Oceans, 129, e2023JC020859, https://doi.org/10.1029/2023JC020859, 2024.

Small, J.: A nonlinear model of the shoaling and refraction of interfacial solitary waves in the ocean. Part II: Oblique refraction across a continental slope and propagation over a seamount, J. Phys. Oceanogr., 31, 3184–3199, https://doi.org/10.1175/1520-0485(2001)031<3184:ANMOTS>2.0.CO;2, 2001.

Tchilibou, M., Gourdeau, L., Lyard, F., Morrow, R., Koch Larrouy, A., Allain, D., and Djath, B.: Internal tides in the Solomon Sea in contrasted ENSO conditions, Ocean Sci., 16, 615–635, https://doi.org/10.5194/os-16-615-2020, 2020.

Tchilibou, M., Koch-Larrouy, A., Barbot, S., Lyard, F., Morel, Y., Jouanno, J., and Morrow, R.: Internal tides off the Amazon shelf during two contrasted seasons: Interactions with background circulation and SSH imprints, Ocean Sci., 18, 1591–1618, https://doi.org/10.5194/os-18-1591-2022, 2022.

Vic, C., Naveira Garabato, A. C., Green, J. M., Waterhouse, A. F., Zhao, Z., Melet, A., de Lavergne, C., Buijsman, M. C., and Stephenson, G. R.: Deep-ocean mixing driven by small-scale internal tides, Nat. Commun., 10, 2099, https://doi.org/10.1038/s41467-019-10149-5, 2019.

Wang, W., Li, J., and Huang, X.: Semidiurnal internal tide interference in the northern South China Sea, J. Marine Sci. Eng., 12, 811, https://doi.org/10.3390/jmse12050811, 2024.

Wang, X., Peng, S., Liu, Z., Huang, R. X., Qian, Y.-K., and Li, Y.: Tidal mixing in the South China Sea: An estimate based on the internal tide energetics, J. Phys. Oceanogr., 46, 107–124, https://doi.org/10.1175/JPO-D-15-0082.1, 2016.

Wang, Y., Curchitser, E., Legg, S., and Kang, D.: Internal tide interactions with submesoscale and mesoscale eddies in the tropical western Atlantic, J. Phys. Oceanogr., 55, 1245–1262, https://doi.org/10.1175/JPO-D-24-0063.1, 2025.

https://doi.org/10.5194/egusphere-2025-6390
Preprint. Discussion started: 30 December 2025

Wang, Y., and Legg, S.: Enhanced dissipation of internal tides in a mesoscale baroclinic eddy, J. Phys. Oceanogr., 53, 2533–2550, https://doi.org/10.1175/JPO-D-22-0205.1, 2023.

Wang, Y., Xu, Z., Hibiya, T., Yin, B., and Wang, F.: Radiation path of diurnal internal tides in the northwestern Pacific controlled by refraction and interference, J. Geophys. Res.: Oceans, 126, e2020JC016972, https://doi.org/10.1029/2020JC016972, 2021.

Weiss, J.: The dynamics of enstrophy transfer in 2-dimensional hydrodynamics, Physica D, 48, 273–294, https://doi.org/10.1016/0167-2789(91)90088-Q, 1991.

Winters, K. B., and D'Asaro, E. A.: Diascalar flux and the rate of fluid mixing, J. Fluid Mech., 317, 179–193, https://doi.org/10.1017/S002211209600007X, 1996.

Wunsch, C., and Ferrari, R.: Vertical mixing, energy, and the general circulation of the oceans, Annu. Rev. Fluid Mech., 36, 281–314, https://doi.org/10.1146/annurev.fluid.36.050802.122121, 2004.

Xu, A., Yu, F., and Nan, F.: Study of subsurface eddy properties in northwestern Pacific Ocean based on an eddy-resolving OGCM, Ocean Dynam., 69, 463–474, https://doi.org/10.1007/s10236-019-01255-5, 2019.

Xu, Z., Liu, K., Yin, B., Zhao, Z., Wang, Y., and Li, Q.: Longrange propagation and associated variability of internal tides in the South China Sea, J. Geophys. Res.-Oceans, 121, 8268–8286, https://doi.org/10.1002/2016JC012105, 2016.

Xu, Z., Wang, Y., Liu, Z., McWilliams, J. C., and Gan, J.: Insight into the dynamics of the radiating internal tide associated with the Kuroshio current, J. Geophys. Res.: Oceans, 126, e2020JC017018, https://doi.org/10.1029/2020JC017018, 2021.

Zhao, Z.: The global mode-2 M2 internal tide, J. Geophys. Res.: Oceans, 123, 7725–7746, https://doi.org/10.1029/2018JC014380, 2018.

Zhao, Z.: Internal tide radiation from the Luzon Strait, J. Geophys. Res.: Oceans, 119, 5434–5448, https://doi.org/10.1002/2014JC010150, 2014.

Zhao, Z., Alford, M. H., MacKinnon, J. A., and Pinkel, R.: Long-range propagation of the semidiurnal internal tide from the Hawaiian Ridge, J. Phys. Oceanogr., 40, 713–736, https://doi.org/10.1175/2009JPO4207.1, 2010.

Zhao, Z.: The global mode-1 S2 internal tide, J. Geophys. Res.-Oceans, 122, 8794–8812, https://doi.org/10.1002/2017JC013112, 2017.

https://doi.org/10.5194/egusphere-2025-6390
Preprint. Discussion started: 30 December 2025

Zalesak, S. T.: Fully multidimensional flux-corrected transport algorithms for fluids, J. Comput. Phys., 31, 335–362, https://doi.org/10.1016/0021-9991(79)90051-2, 1979.

Zaron, E. D., and Egbert, G. D.: Time-variable refraction of internal tides at the Hawaiian Ridge, J. Phys. Oceanogr., 44, 538–557, https://doi.org/10.1175/JPO-D-12-0238.1, 2014.

Appendix

Appendix A: M_2 Tidal Beam Dynamics

To better determine whether the response of ITs to MEs, specifically CEs, is governed more by the IT's vertical structure or by the CE's properties and location, we analyzed the M2 baroclinic velocity field. Following the methodology in Sect. 2.2.2, we projected the velocity field into vertical modes and defined transects along different IT beams for the NE, CEC, and CEE cases (Fig. A1): the northeastward incident beam (yellow) from sites A and D, northward refracted beams from CE center (green), and diffracted beams (northward and eastward) from CE periphery (green). We then decomposed the modal velocities into along- and cross-transect components. The transect along the incident tidal beam was identical in all three cases to enable a direct comparison. Our analysis focused on the more energetic along-transect component, as shown in Figs. A2-A4. The vertical structure of this velocity component was found to be coherent with the modal M2 energy flux patterns in all analyzed cases.

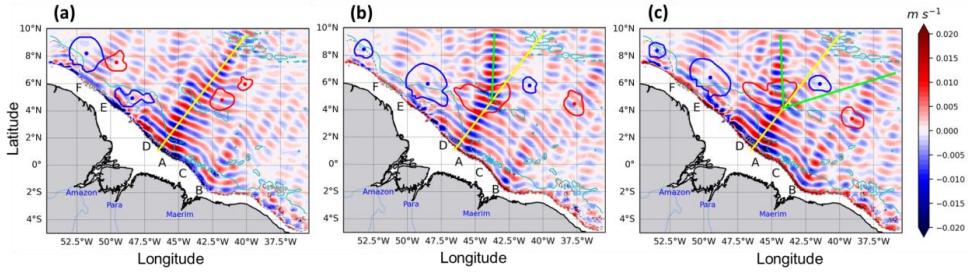

Figure A1. Horizontal propagation of mode-1 M2 IT beams. Snapshots (at t = 6 h) of meridional baroclinic velocity for the (a) NE, (b) CEC, and (c) CEE cases. The corresponding dates are 24 November 2015, 17 September 2015, and 29 September 2015, respectively. All panels include defined transects along different IT beams: the northeastward incident beam (yellow) from sites A and D, northward refracted beams from CE core (green), and diffracted beams (northward and eastward) from CE periphery (green). Detected eddy edges (closed contours) and centroids (dots) for AE (blue) and CE (red) are also shown.

https://doi.org/10.5194/egusphere-2025-6390
Preprint. Discussion started: 30 December 2025

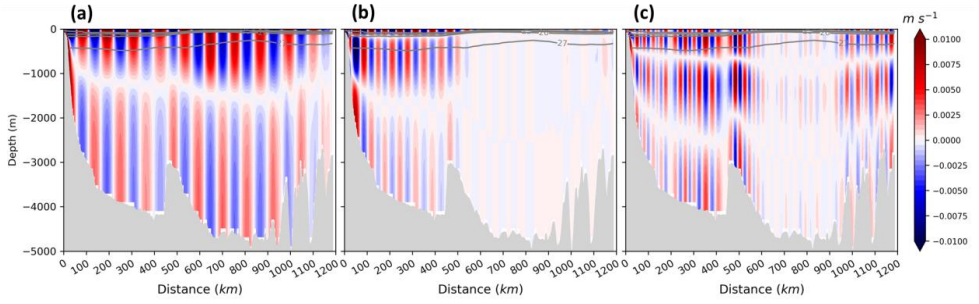

Figure A2. Vertical structure of the first three M2 IT modes in the NE case. Snapshots (t = 6 h on 24 November 2015) of the along-transect baroclinic velocity component for modes 1 (a), 2 (b), and 3 (c) along the northeastward incident beam. All panels include selected potential density isopycnals (23–27 kg m^{-3}, grey contours), and the seafloor topography (grey shading).

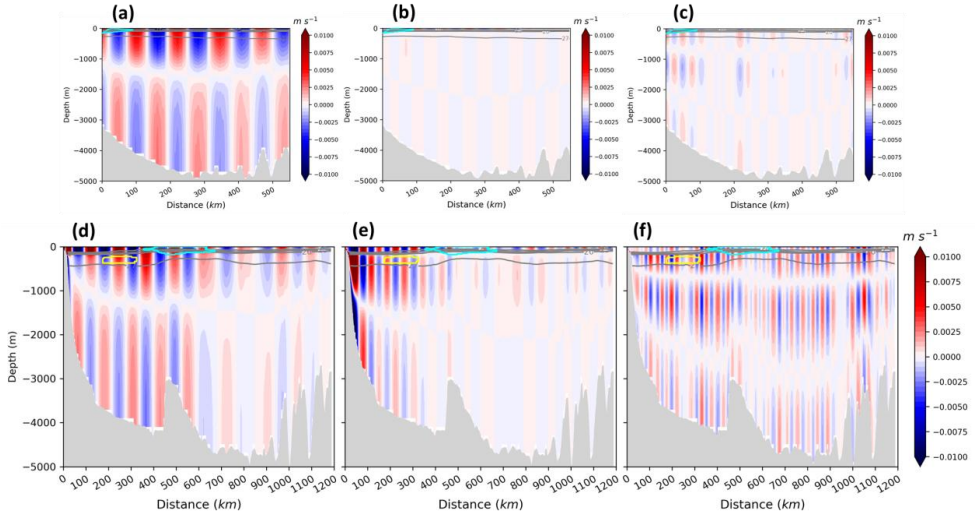

Figure A3. Vertical structure of the first three M2 IT modes in the CEC case. Snapshots (t = 6 h on 17 September 2015) of the along-transect baroclinic velocity component for modes 1 (a, d), 2 (b, e), and 3 (c, f) along different beams: the northward diffracted beam (a-c) and the northeastward incident beam (d-f). All panels include detected eddy edges for AE (yellow) and CE (cyan), selected potential density isopycnals (23–27 kg m^{-3}, grey contours), and the seafloor topography (grey shading).

https://doi.org/10.5194/egusphere-2025-6390
Preprint. Discussion started: 30 December 2025

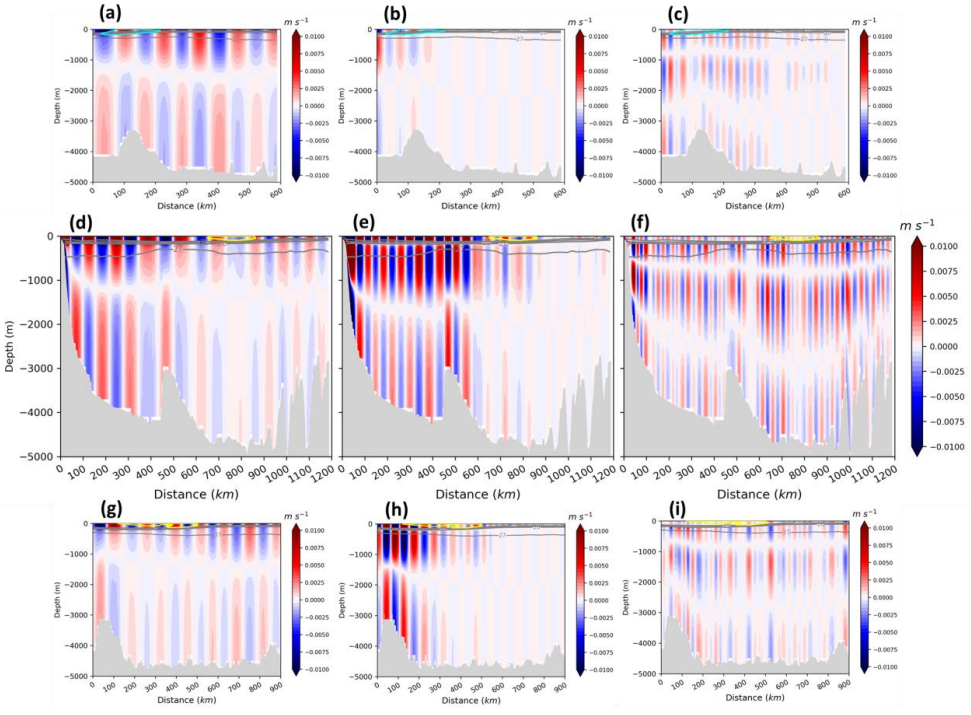

Figure A4. Vertical structure of the first three M2 IT modes in the CEE case. Snapshots (t = 6 h on 29 September 2015) of the along-transect baroclinic velocity component for modes 1 (a, d, g), 2 (b, e, h), and 3 (c, f, i) along different beams: the northward diffracted beam (a-c), the northeastward incident beam (d-f), and the eastward diffracted beam (g-i). All panels include detected eddy edges for AE (yellow) and CE (cyan) eddies, selected potential density isopycnals (23–27 kg m^{-3}, grey contours), and the seafloor topography (grey shading).